Discovery of Radio Recombination Lines from Proplyds in the Orion Nebula Cluster

N.B. When citing this work, cite the original published paper.

(article starts on next page)

Discovery of Radio Recombination Lines from Proplyds in the Orion Nebula Cluster

Ryan D. Boyden[1,2,7] , Kimberly L. Emig[3] , Nicholas P. Ballering[1,2] , Charles J. Law[1,8] , Thomas J. Haworth[4] ,
Jonathan C. Tan[1,5] , L. Ilsedore Cleeves[1,6] , and Zhi-Yun Li[1]

[1] Department of Astronomy, University of Virginia, Charlottesville, VA 22904, USA; rboyden@virginia.edu
[2] Space Science Institute, Boulder, CO 80301, USA
[3] National Radio Astronomy Observatory, Charlottesville, VA 22903, USA
[4] Astronomy Unit, School of Physics and Astronomy, Queen Mary University of London, London E1 4NS, UK
[5] Department of Space, Earth and Environment, Chalmers University of Technology, SE-41296 Gothenburg, Sweden
[6] Department of Chemistry, University of Virginia, Charlottesville, VA 22904, USA
Received 2024 December 6; revised 2025 February 18; accepted 2025 February 28; published 2025 April 9

Abstract

We present new Atacama Large Millimeter/submillimeter Array observations that, for the first time, detect hydrogen and helium radio recombination lines from a protoplanetary disk. We imaged the Orion Nebula Cluster at 3.1 mm with a spectral setup that covered the $n = 42 \to 41$ transitions of hydrogen (H41α) and helium (He41α). The unprecedented sensitivity of these observations enables us to search for radio recombination lines toward the positions of $\sim$200 protoplanetary disks. We detect H41α from 17 disks, all of which are HST-identified "proplyds." The detected H41α emission is spatially coincident with the locations of proplyd ionization fronts, indicating that proplyd H41α emission is produced by gas that has been photoevaporated off the disk and ionized by UV radiation from massive stars. We measure the fluxes and widths of the detected H41α lines and find line fluxes of $\sim$30–800 mJy km s^{-1} and line widths of $\sim$30–90 km s^{-1}. The derived line widths indicate that the broadening of proplyd H41α emission is dominated by outflowing gas motions associated with external photoevaporation. The derived line fluxes, when compared with measurements of 3.1 mm free–free flux, imply that the ionization fronts of H41α-detected proplyds have electron temperatures of $\sim$6000–11,000 K and electron densities of $\sim$10^6–10^7 cm^{-3}. Finally, we detect He41α toward one H41α-detected source and find evidence that this system is helium-rich. Our study demonstrates that radio recombination lines are readily detectable in ionized photoevaporating disks, providing a new way to measure disk properties in clustered star-forming regions.

Unified Astronomy Thesaurus concepts: Proplyds (1296); Protoplanetary disks (1300); Planet formation (1241); Photoionization (2060); Submillimeter astronomy (1647); Radio astronomy (1338); Young star clusters (1833); Radio interferometry (1346)

1. Introduction

Planets form in protoplanetary disks around young stars (e.g., M. Keppler et al. 2018), and the properties of emerging planetary systems depend intimately on the structure, composition and evolution of protoplanetary disks (K. I. Öberg & E. A. Bergin 2021; K. I. Öberg et al. 2023). The majority of stars, including the Sun, are born in dense, massive clusters (E. A. Lada et al. 1993; C. J. Lada & E. A. Lada 2003; F. C. Adams 2010; M. R. Krumholz et al. 2019; E. A. Bergin et al. 2023). Understanding how disks evolve in clustered star-forming regions is crucial to interpreting the demographics of disks and exoplanets.

Theoretically, there is an expectation that the radiation environments of clusters influence disk properties (for recent reviews, see R. J. Parker 2020; A. J. Winter & T. J. Haworth 2022). Clusters host massive OB stars that irradiate their surroundings with UV photons. This intense radiation heats and ionizes protoplanetary disks in the cluster, driving material off their surfaces in the form of photoevaporative winds (e.g.,

D. Johnstone et al. 1998). The external photoevaporation of disks is predicted to dominate over other internal and external mechanisms of disk dispersal in a range of cluster environments (e.g., A. Scally & C. Clarke 2001; A. J. Winter et al. 2018, 2020; F. Concha-Ramírez et al. 2021, 2023; G. A. L. Coleman & T. J. Haworth 2022; G. A. L. Coleman et al. 2024; A. Gautam et al. 2025), leading to rapid disk truncation, intense mass loss, warmer disk temperatures, and shorter disk lifetimes in comparison with disks in lower-density star-forming regions (e.g., F. C. Adams et al. 2004; C. J. Clarke 2007; Y. G. Tsamis et al. 2013; C. Walsh et al. 2013; S. Facchini et al. 2016; T. J. Haworth et al. 2018a; F. Concha-Ramírez et al. 2019; T. J. Haworth & C. J. Clarke 2019; T. J. Haworth 2021; R. D. Boyden & J. A. Eisner 2023; M. Gárate et al. 2024; N. P. Ballering et al. 2025). If the extinction levels in clusters decline rapidly, such that disks become externally irradiated at early evolutionary stages (e.g., L. Qiao et al. 2022; M. J. C. Wilhelm et al. 2023), then external photoevaporation has the potential to influence both early- and late-stage planet formation (e.g., H. B. Throop & J. Bally 2005; T. J. Haworth et al. 2018b; N. Ndugu et al. 2018; A. J. Winter et al. 2022), or even suppress the formation of planets altogether (e.g., R. B. Nicholson et al. 2019; R. J. Parker et al. 2021b; L. Qiao et al. 2023; S. Huang et al. 2024).

The Orion Nebula Cluster (ONC) provides one of the most compelling sites to study external photoevaporation. At a distance of 400 pc (T. Hirota et al. 2007; S. Kraus et al. 2007; K. M. Menten et al. 2007; K. M. Sandstrom et al. 2007;

M. Kounkel et al. 2017; J. E. Großschedl et al. 2018; M. Kounkel et al. 2018), it is the nearest and most readily observable high-mass cluster, comprising thousands of young (1–2 Myr) low-mass ($<2 M_\odot$) stars (L. A. Hillenbrand 1997; M. Fang et al. 2021) that are irradiated by the massive Trapezium stars, most notably the O6V star θ^1 Ori C. In comparison with other nearby clusters, the ONC contains the largest population of disks with direct evidence of ongoing external photoevaporation. These disks, typically referred to as "proplyds," consist of a central disk surrounded by a cocoon of ionized gas with a cometary morphology (e.g., C. R. O'dell & Z. Wen 1994; J. Bally et al. 1998; L. Ricci et al. 2008). The cometary morphologies of proplyds arise from material being photoevaporated off the disk surfaces by external UV radiation (D. Johnstone et al. 1998). For most proplyds, the photoevaporative winds are driven by far-ultraviolet (FUV) radiation and then ionized by extreme-ultraviolet (EUV) radiation at an ionization front that is separated from the disk surface (e.g., H. Störzer & D. Hollenbach 1999; S. Richling & H. W. Yorke 2000). For the proplyds closest to θ^1 Ori C (i.e., within $\lesssim 0.03$ pc), the EUV radiation is strong enough to overpower the FUV radiation and drive external photoevaporation, in which case the ionization front is closer to the disk surface than in the FUV-driven case (e.g., D. Johnstone et al. 1998).

More than 200 proplyds have been identified in the ONC with optical (e.g., C. R. O'dell & Z. Wen 1994; J. Bally et al. 1998, 2000; L. Ricci et al. 2008; M.-L. Aru et al. 2024), infrared (e.g., E. Habart et al. 2024; M. J. McCaughrean & S. G. Pearson 2023), millimeter (e.g., J. A. Eisner et al. 2008; R. K. Mann et al. 2014), and radio imaging (e.g., E. Churchwell et al. 1987; G. Garay et al. 1987; L. A. Zapata et al. 2004; J. Forbrich et al. 2016; P. D. Sheehan et al. 2016). The detected proplyds span a range of morphologies, disk masses, and stellar properties, though the majority appear to host compact disks with sizes smaller than a hundred au (e.g., R. K. Mann et al. 2014; J. A. Eisner et al. 2018; R. D. Boyden & J. A. Eisner 2020; J. Otter et al. 2021; N. P. Ballering et al. 2023). The prevalence, diversity, and proximity of the ONC's proplyd population allows for a unique opportunity to constrain the relationships between external photoevaporation, star cluster evolution, and planet formation. Detailed spectroscopic studies at optical and infrared wavelengths have enabled constraints on the densities, temperatures, kinematics, and chemical compositions of photoevaporative winds for a handful of disk-proplyd systems (W. J. Henney & C. R. O'Dell 1999; W. J. Henney et al. 2002; M. J. Vasconcelos et al. 2005; Y. G. Tsamis & J. R. Walsh 2011; Y. G. Tsamis et al. 2011, 2013; A. Mesa-Delgado et al. 2012; J. E. Méndez-Delgado et al. 2022; A. Kirwan et al. 2023; O. Berné et al. 2024; J. R. Goicoechea et al. 2024; M. Zannese et al. 2024). However, to obtain a comprehensive picture of how external photoevaporation proceeds in a clustered star-forming environment, spectroscopic observations targeting larger and more diverse samples of photoevaporating disks are essential.

In this paper, we present new Atacama Large Millimeter/ submillimeter Array (ALMA) observations that, for the first time, detect hydrogen and helium radio recombination lines from proplyds in the ONC. Radio recombination lines are electronic spectral line transitions associated with high principal quantum numbers; they are emitted when a free electron recombines with an ion and passes through high-

quantum-number energy levels while cascading down to lower energy levels (M. A. Gordon & R. L. Sorochenko 2009; B. T. Draine 2011). For decades, radio recombination lines have been used to measure the densities, temperatures, kinematics, and chemistry of H II regions (see review in E. Churchwell 2002). With our deep, high-resolution ALMA observations, we can build upon studies of H II regions and use radio recombination lines to measure the physical conditions of a sample of photoevaporating protoplanetary disks.

2. Observations and Data Reduction

Our Cycle 6 ALMA Program mapped the ONC at Band 3 (3.1 mm). Observations were taken on 2019 July 7 and 2019 July 9 under project code 2018.1.01107.S. The C43-9 configuration was utilized to mosaic the central $2'.0 \times 2'.5$ of the ONC with 10 pointings, covering baselines ranging from 149 m to 13.9 km with total on-source integration times of $\sim$16 minutes per pointing. The spectral setup consisted of four windows centered at 90.5, 92.4, 102.5, and 104.4 GHz, with each window having a bandwidth of 1.875 GHz and channel spacing of 976.562 kHz ($\sim$3.5 km s^{-1}). The hydrogen $n = 42 \rightarrow 41$ (H41α) and helium $n = 42 \rightarrow 41$ (He41α) recombination lines, with rest frequencies of 92.034 and 92.072 GHz, were covered in the 92.4 GHz window. N. P. Ballering et al. (2023) presented the aggregate 3.1 mm continuum images produced from these ALMA observations, along with a full description of the continuum data reduction and imaging procedures. Below, we summarize our procedure for generating radio recombination line spectral cubes from these observations.

We began by retrieving the pipeline-calibrated measurement sets from the ALMA archive; data were downloaded and restored with the required pipeline version of CASA (5.4.0-70). We then used CASA version 6.5.4.9 for additional data processing. We used the `uvcontsub` task to fit and remove the continuum with a first-order polynomial. We then used the `split` task to create standalone measurement sets for the continuum-subtracted 92.4 GHz spectral window, as this window includes our spectral lines of interest (i.e., H41α and He41α).

We imaged the continuum-subtracted measurement sets together using the `tclean` task with *specmode = cube*. We centered the image cube about the rest frequency of H41α and generated velocity channels in the range ± 200 km s^{-1}. This velocity range was sufficient to cover emission from both H41α and He41α, the latter of which, at rest, is about -122 km s^{-1} away from the H41α line.

All mosaic pointings were imaged together using the mosaic gridder with a phase center R.A. of 05:35:16.578 and decl. of −05:23:12.150, i.e., the same phase center used by N. P. Ballering et al. (2023) for the continuum imaging. To determine the positions of CLEAN boxes, we employed an iterative process where we first placed $1'' \times 1''$ CLEAN boxes around all objects detected above 8σ, generated a CLEANed image, searched the residuals for detections above 4σ, and then generated a new CLEANed image with additional $1'' \times 1''$ CLEAN boxes placed around additional detections. Each CLEAN box was applied uniformly in all channels, and we employed a 2σ threshold to mitigate CLEANing of noise spikes. Imaging parameters were chosen to prioritize the signal-to-noise ratio (S/N) over spatial resolution. For our final imaging, we utilized a multiscale deconvolver with pixel scales of [0, 5, 15], natural weighting, and a *uv* taper of $0''.1$. We did

not perform the self-calibration and artifact removal procedure described in N. P. Ballering et al. (2023), which marginally improved the continuum rms in the vicinity of θ^1 Ori A, BN, and Src I. These continuum sources do not produce strong artifacts in our continuum-subtracted line data cubes; we find that the cube rms is more spatially correlated with primary beam value than with proximity to bright continuum sources.

Our final data products consist of two CLEANed data cubes, one binned into $3.5\ \mathrm{km\ s^{-1}}$ channels (i.e., the approximate spectral resolution), and another binned into $10\ \mathrm{km\ s^{-1}}$ channels. The coarser-binned data cube achieves higher S/N and is used to search for H41α and He41α detections (see Sections 3.1 and 3.2). The finer-binned data cube is used to derive source properties from spectral line fitting (see Section 3.3). In most regions of our cubes, the rms noise in an individual velocity channel is ~ 0.45–$0.55\ \mathrm{mJy\ beam^{-1}}$ in our coarser-binned ($10\ \mathrm{km\ s^{-1}}$ channels) cube and ~ 0.65–$0.75\ \mathrm{mJy\ beam^{-1}}$ in our finer-binned ($3.5\ \mathrm{km\ s^{-1}}$ channels) cube. In the outer regions of our cubes, the rms increases to values of $\sim 1\ \mathrm{mJy\ beam^{-1}}$.

The synthesized beam size for our cubes is about $\sim 0\rlap{.}''2$. This beam size is ~ 3 times larger than the beam size achieved by N. P. Ballering et al. (2023) for the 3.1 mm continuum image ($\sim 0\rlap{.}''07$). At the 400 pc distance to Orion (T. Hirota et al. 2007; S. Kraus et al. 2007; K. M. Menten et al. 2007; K. M. Sandstrom et al. 2007; M. Kounkel et al. 2017, 2018; J. E. Großschedl et al. 2018), a beam size of $\sim 0\rlap{.}''2$ corresponds to a spatial resolution of about ~ 80 au.

3. Results

3.1. H41α Detections

To identify H41α emission from protoplanetary disks, we perform a detection search toward the positions of the 271 sources detected in the 3.1 mm continuum by N. P. Ballering et al. (2023) and N. P. Ballering et al. (2025, in preparation). We use our $10\ \mathrm{km\ s^{-1}}$ channel data cube to search for H41α detections. We consider H41α to be detected in the channel maps if emission within $0\rlap{.}''5$ of the known source position is detected at $>4\sigma$ in at least three consecutive velocity channels within $\pm 60\ \mathrm{km\ s^{-1}}$ of the H41α rest frequency. This velocity range more than covers the systemic velocities of ONC members. If H41α is not detected in the channel maps, then we compute moment 0 (integrated intensity) maps and spectra to see if it can be detected at $>4\sigma$ in a spatially or spectrally integrated frame. Our detection search is conducted manually using the search guidelines listed above. Our final detection count includes sources detected in the full channel maps as well as sources detected in the spatially and/or spectrally integrated frame only.

Table 1 lists the coordinates and names of all sources detected in H41α. We detect H41α emission from 17 protoplanetary disks. Of these 17 sources, 14 are detected at $>4\sigma$ in the channel maps, and 3 are detected at $>4\sigma$ in the moment 0 maps only (sources 166–316, 159–350, and 176–325). All 17 detections are HST-identified proplyds from the L. Ricci et al. (2008) catalog. Five are proplyds that were presented in N. P. Ballering et al. (2023) as 3.1 mm detections with spatially isolated disks and ionization fronts, and the rest are compact proplyds whose mm continuum is dominated by free–free emission from the ionization front (see example spectral energy distributions in R. K. Mann et al. 2014;

J. A. Eisner et al. 2018). Two proplyds, 168–326 SE and 168–326 NW, are within $0\rlap{.}''3$ of each other and detected as a single object in our $0\rlap{.}''2$ resolution data cubes. For the remainder of this paper, we treat 168–326 SE and 168–326 NW as a single H41α-detected source, which we refer to as 168–326 SE/NW. In Appendix A, we show 3.1 mm continuum subimages of each H41α-detected proplyd.

Figure 1 shows the locations of the H41α-detected proplyds. The detections are concentrated in the center of the ONC near the massive Trapezium stars. Eleven are within ~ 0.03 pc (in projected separation) of θ^1 Ori C, where external photoevaporation is thought to be driven by EUV radiation rather than FUV radiation (D. Johnstone et al. 1998; H. Störzer & D. Hollenbach 1999). The other five detections have projected separations of ~ 0.03–0.06 pc and are instead in regions where external photoevaporation is likely driven by FUV radiation. We note that the five detections with projected separations between 0.03 and 0.06 pc are all in the same local region to the south of θ^1 Ori C. These proplyds may be closer to θ^1 Ori C and thus exposed to stronger EUV fields than other proplyds with similar projected separations but different local positions in the ONC.

Figure 2 shows moment 0 maps of H41α for the detected proplyds. The detected H41α emission is intimately associated with the locations of the resolved ionization fronts. For the extended proplyds whose disks and ionization fronts are spatially separated in the 3.1 mm continuum (e.g., 177–341W, 158–327, and 159–350), the H41α emission is concentrated toward the ionization front rather than the central disk. For the compact proplyds whose 3.1 mm morphologies are dominated by the ionization fronts, (e.g., 167–317, 158–323, and 161–234), the H41α emission is detected over the majority of positions where 3.1 mm continuum emission is seen.

Figure 3 shows moment 1 (intensity-weighted velocity) maps of H41α for the detected proplyds. Many detections have H41α velocity gradients that are marginally detected at our current sensitivity and resolution. For proplyds 158–323, 161–324, 168–328, 163–323, 171–334, 177–341W, 159–338, and 170–337, the moment 1 maps show linear velocity gradients across the mm-identified ionization fronts. Photoevaporative winds can produce linear velocity gradients when the outflowing gas is rotating and/or reoriented along different flow directions while passing through an ionization front (e.g., S. Richling & H. W. Yorke 2000; T. J. Haworth & J. E. Owen 2020), so the detection of linear velocity gradients is consistent with the H41α emission being produced by an externally ionized disk wind. For proplyds 167–316, 168–326 SE/NW, 163–317, 158–327, and 180–331, the moment 1 maps reveal more complex features that deviate from a single velocity gradient. These deviations can be produced by photoevaporative disk winds with face-on orientations (e.g., T. J. Haworth & J. E. Owen 2020); however, they can also be explained by a combination of disk-wind and jet emission (e.g., P. D. Klaassen et al. 2018; L. Moscadelli et al. 2021). Finally, toward 166–316, 159–350, and 176–325, no clear velocity gradient is seen.

Figure 4 shows spectra for the H41α-detected proplyds. We extract spectra using circular apertures that are centered about the coordinates of each source. For 168–326 SE/NW, we place apertures around 168–326 SE and 168–326 NW and sum the emission contained in both apertures. Aperture sizes are determined on a source-by-source basis and defined as the
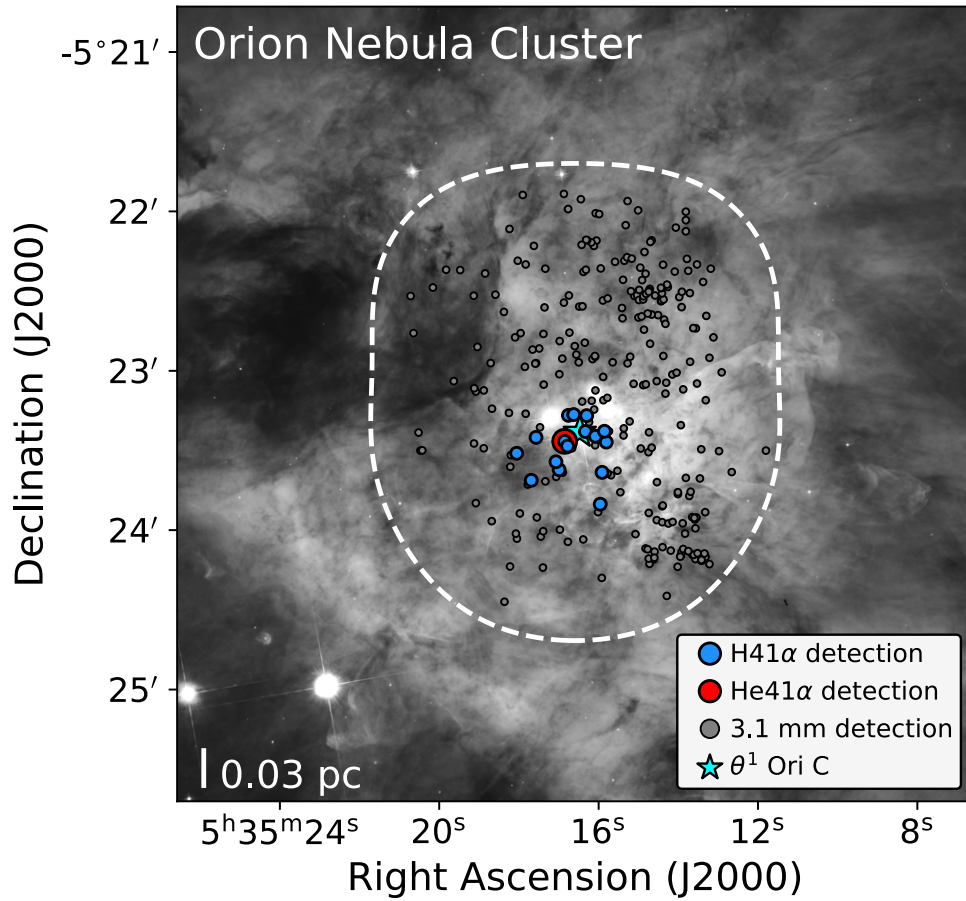
Figure 1. The Orion Nebula Cluster, as seen with HST/Advanced Camera for Surveys (L. Ricci et al. 2008). The white dashed line depicts the field of view of our 3.1 mm ALMA mosaic. Blue circles indicate proplyds detected in H41α. The red circle marks the proplyd that is also detected in He41α. Gray circles indicate the positions of 3.1 mm continuum detections that are not detected in H41α or He41α. The cyan star indicates the position of the ionizing source θ^1 Ori C.

Table 1
Properties of Sources Detected in H41α

ID	R.A. (J2000)	Decl. (J2000)	$d_{\theta^1 C}$ (pc)	$D_{aperture}$ (arcsec)	$Amp_{H41\alpha}$ (mJy)	$v_{cen,H41\alpha}$ (km s^{-1})	$\Delta v_{H41\alpha}$ (km s^{-1})	$\int S_{H41\alpha}\, dV$ (mJy km s^{-1})
(1)	(2)	(3)	(4)	(5)	(6)	(7)	(8)	(9)
167–317	05:35:16.75	−05:23:16.48	0.015	0.54	11.36 ± 0.66	9.44 ± 1.65	58.15 ± 3.88	703 ± 62
168–326 SE/NW[a]	05:35:16.84	−05:23:26.29	0.013	0.6	15.25 ± 0.85	15.97 ± 1.24	45.29 ± 2.91	735 ± 63
163–317	05:35:16.29	−05:23:16.58	0.013	0.48	7.64 ± 0.58	10.94 ± 1.67	44.96 ± 3.94	366 ± 42
158–323	05:35:15.84	−05:23:22.47	0.018	0.51	5.63 ± 0.57	16.33 ± 2.57	51.96 ± 6.06	311 ± 48
161–324	05:35:16.07	−05:23:24.38	0.012	0.42	3.73 ± 0.38	3.92 ± 2.86	56.44 ± 6.72	224 ± 35
168–328	05:35:16.77	−05:23:28.08	0.014	0.33	2.08 ± 0.29	16.60 ± 2.44	35.73 ± 5.74	79 ± 17
163–323	05:35:16.32	−05:23:22.57	0.004	0.36	2.24 ± 0.35	−1.01 ± 3.67	48.65 ± 8.64	116 ± 27
171–334	05:35:17.06	−05:23:34.01	0.028	0.45	2.77 ± 0.41	5.29 ± 2.91	40.10 ± 6.85	118 ± 27
177–341W[b]	05:35:17.68	−05:23:40.97	0.050	0.9	6.18 ± 0.90	2.37 ± 3.18	44.33 ± 7.48	292 ± 65
158–327[b]	05:35:15.79	−05:23:26.56	0.021	0.75	7.48 ± 0.85	12.10 ± 2.20	39.62 ± 5.19	316 ± 55
159–338	05:35:15.90	−05:23:37.96	0.033	0.66	5.07 ± 0.69	12.44 ± 2.39	35.80 ± 5.62	193 ± 40
180–331[b]	05:35:18.05	−05:23:30.81	0.049	0.63	3.64 ± 0.46	22.67 ± 5.36	86.17 ± 12.62	334 ± 65
170–337[b]	05:35:16.98	−05:23:37.05	0.032	0.45	2.22 ± 0.38	−0.81 ± 5.66	67.58 ± 13.34	159 ± 42
166–316	05:35:16.62	−05:23:16.15	0.014	0.21	0.76 ± 0.15	10.97 ± 4.20	42.99 ± 9.89	35 ± 11
159–350[b]	05:35:15.95	−05:23:50.04	0.055	1.02	8.73 ± 1.17	3.18 ± 2.49	38.01 ± 5.87	353 ± 72
176–325	05:35:17.56	−05:23:24.85	0.032	0.3	1.02 ± 0.20	3.63 ± 4.70	49.70 ± 11.06	54 ± 16

Notes. Column (1): proplyd name. Columns (2) and (3): source coordinates. Column (4): projected distance from θ^1 Ori C. Column (5): circular aperture diameters used to extract radio recombination line spectra. Columns (6), (7), and (8): best-fit H41α peak line flux, central velocity, and line width, derived by fitting Gaussian line profiles to the extracted spectra. Line widths are taken as the Gaussian full width at half maximum. Column (9): integrated H41α line flux, obtained by integrating over the best-fit Gaussian line profiles.

[a] 168–326 SE/NW consists of two individual proplyds, 168–326 SE and 168–326 NW, whose H41α emission is blended together in our 0.″2 resolution data cubes. In Columns (2) and (3), we use the coordinates of 168–326 SE to indicate the position of 168–326 SE/NW.

[b] Indicates a proplyd whose disks and ionization fronts were spatially isolated in the 3.1 mm continuum by N. P. Ballering et al. (2023).
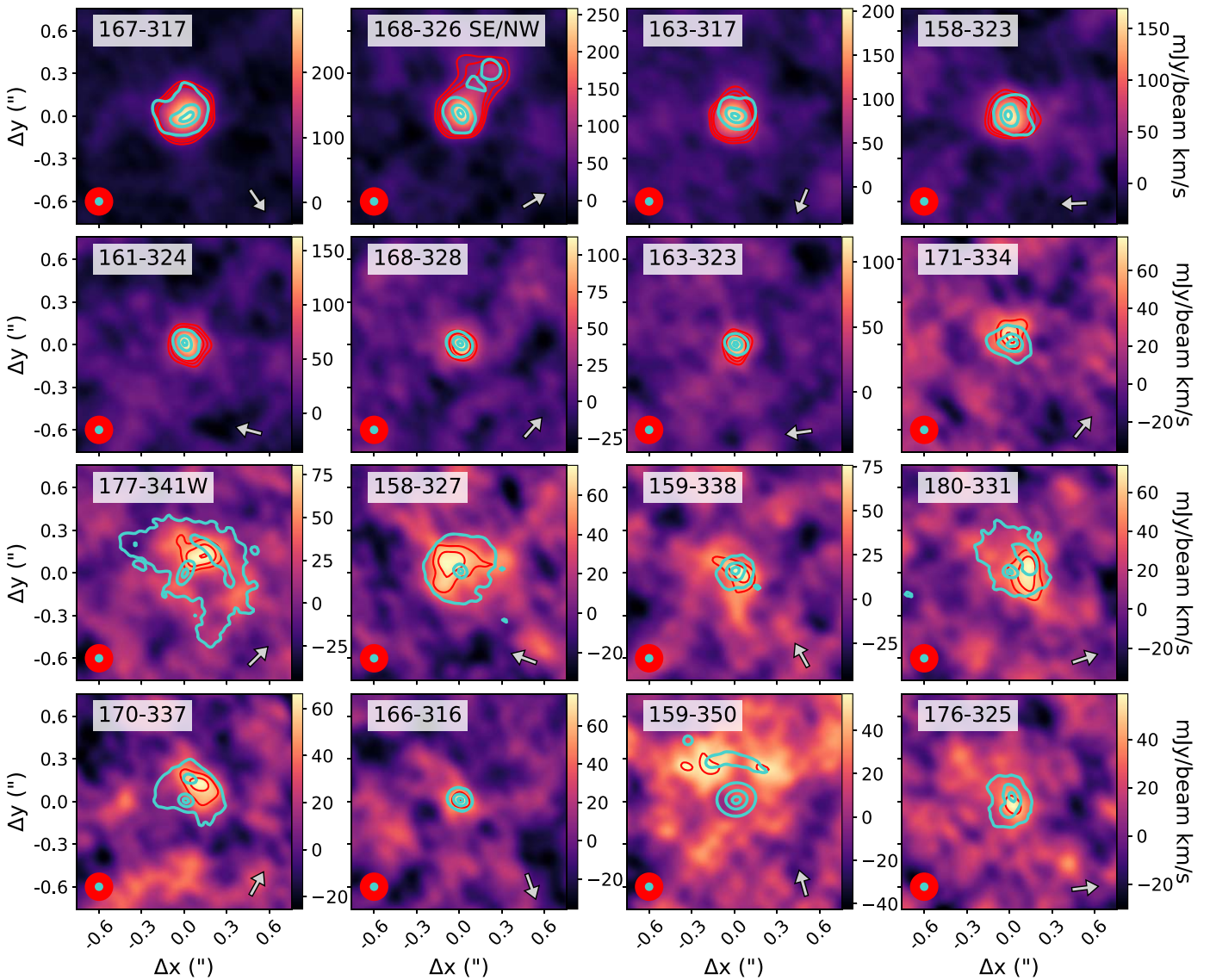
Figure 2. Moment 0 (integrated intensity) maps of H41α for H41α-detected proplyds in the ONC. Each panel corresponds to a 1″.5 × 1″.5 (600 au × 600 au) region centered around each proplyd. Red contours show 3.5σ, 4.5σ, and 5.5σ H41α emission. Teal contours show 3.1 mm continuum emission from N. P. Ballering et al. (2023), with contours drawn at 10%, 50%, and 90% of the maximum continuum flux. The synthesized beams for the 3.1 mm continuum (teal) and H41α (red) images are shown in the lower left corner of each panel. The name of each proplyd is specified in the top left corner of each panel. In the bottom right corner of each panel, we include an arrow that points to the direction of the ionizing source θ¹ Ori C. All moment 0 maps are computed from our data cube with 10 km s⁻¹ channels. We generate moment 0 maps using velocity channels ranging from 0 to 60 km s⁻¹ with respect to the H41α rest frequency. Standalone 3.1 mm continuum images for each proplyd can be found in Appendix A.

diameter that encapsulates all >3σ H41α moment 0 emission associated with a source. We have verified that small (~0″.1) adjustments to the aperture size have a negligible impact on the resulting spectra. In Table 1, we list the final aperture sizes used for each source. Typically, the brightest H41α detections have the most pronounced spectral amplitudes (e.g., 167–317, 168–326 SE/NW); however, a couple of extended, low-surface-brightness detections have amplitudes similar to those of the bright H41α detections (e.g., 159–350).

3.2. He41α Detections

We detect He41α at >4σ toward one H41α detected source: 168–326 SE/NW. In Figure 4, the detected He41α line is seen as a secondary peak at ν ≈ 100 km s⁻¹. Figure 5 shows a moment 0 map of He41α for 168–326 SE/NW. The detected He41α emission follows a morphology similar to that of the

detected H41α emission. Both 168–326 NE and 168–326 SW appear to be detected in He41α, but their emission is blended in our observations, similarly to what is seen with H41α.

3.3. Spectral Line Fitting

We measure the line fluxes, line widths, and central velocities of the detected H41α and He41α lines by fitting Gaussian line profiles to the observed spectra. For proplyd 168–326 SE/NW, we fit two Gaussians in order to reproduce emission from both He41α and H41α. For all other proplyds, we fit a single Gaussian. All best-fit Gaussian parameters and their uncertainties are derived using the Levenberg–Marquardt procedure implemented in `pyspeckit` (A. Ginsburg et al. 2022). Tables 1 and 2 list the best-fit peak line fluxes, line widths, central velocities, and integrated line fluxes for H41α
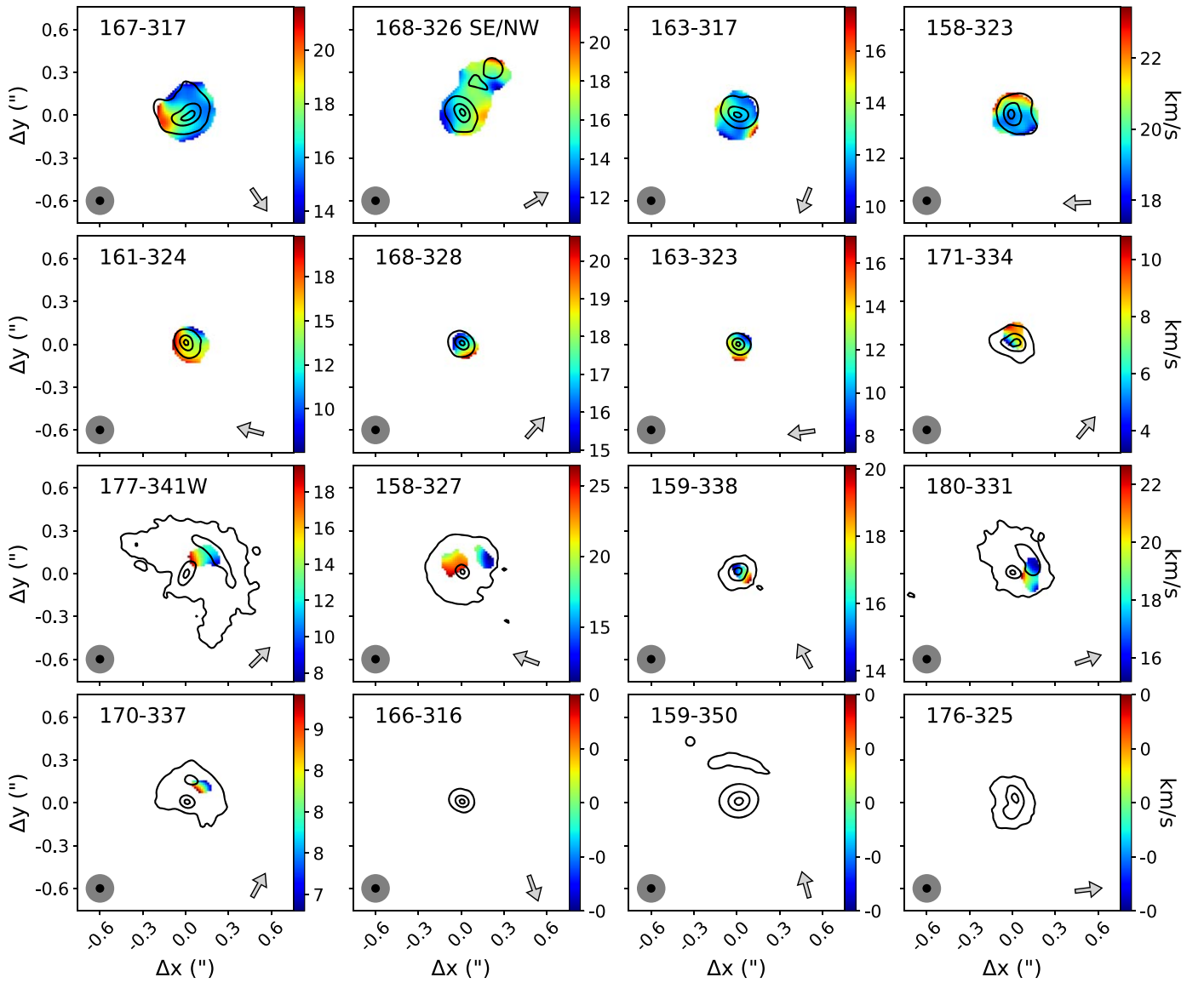
Figure 3. Moment 1 (intensity-weighted velocity) maps of H41α for the H41α-detected proplyds, generated from $\geqslant 4.5\sigma$ channel map emission over the same velocities used to create the moment 0 maps (see Figure 2). The layout of this plot to similar to that of Figure 2, except here we use black contours to show the 3.1 continuum emission, gray circles to show the synthesized beam for H41α, and black circles to show the synthesized beam for the 3.1 mm continuum. All moment 1 maps are generated from our data cube with 10 km s^{-1} channels.

and He41α, respectively. Table 2 also provides the integrated line flux ratio of He41α to H41α for 168–326 SE/NW.

The detected H41α lines span an order of magnitude in flux, with peak line fluxes ranging from $\sim$1 to $\sim$15 mJy, and integrated line fluxes ranging from $\sim$30 to $\sim$800 mJy km s^{-1}. The H41α central velocities tend to be around 0 to $\sim$20 km s^{-1}, which is consistent with the local standard of rest velocities measured toward individual proplyds in the ONC (e.g., J. Bally et al. 2015; S. M. Factor et al. 2017; R. D. Boyden & J. A. Eisner 2020, 2023). For 168–328 SE/NW, the rest-frame H41α and He41α central velocities are within $\sim$2σ of each other, and the integrated line flux ratio of He41α to H41α is $\sim$0.2, which is about two times larger than the typical values seen in most, but not all, Galactic H II regions (e.g., E. Churchwell et al. 1974; D. A. Roshi et al. 2017; R. Galván-Madrid et al. 2024). For the line widths, we typically derive the full widths at half maximum of $\sim$40–60 km s^{-1} for H41α and $\sim$20 km s^{-1} for He41α. In

general, these line widths are consistent with, but somewhat broader than, the line widths measured toward proplyds with optical recombination lines (e.g., W. J. Henney & C. R. O'Dell 1999). Finally, 180–331 has a best-fit H41α line width that is significantly broader than the typical values measured across our sample; though, at our current sensitivity and resolution, it is unclear whether this is driven by a low signal-to-noise ratio.

While the detected H41α and He41α lines are fit well by Gaussians, we note that radio recombination lines can also exhibit Voigt line profiles when they are influenced by pressure broadening (e.g., E. Keto et al. 2008). We have performed Voigt profile fitting to check whether any detected lines are fit better by Voigt than by Gaussian profiles. We find that the derived line profiles are qualitatively similar and yield similar reduced χ^2 values (see example in Appendix B). However, at our current sensitivity and spectral resolution, we are typically unable to reliably constrain the Gaussian and Lorentzian components of the Voigt profiles, because in the velocity
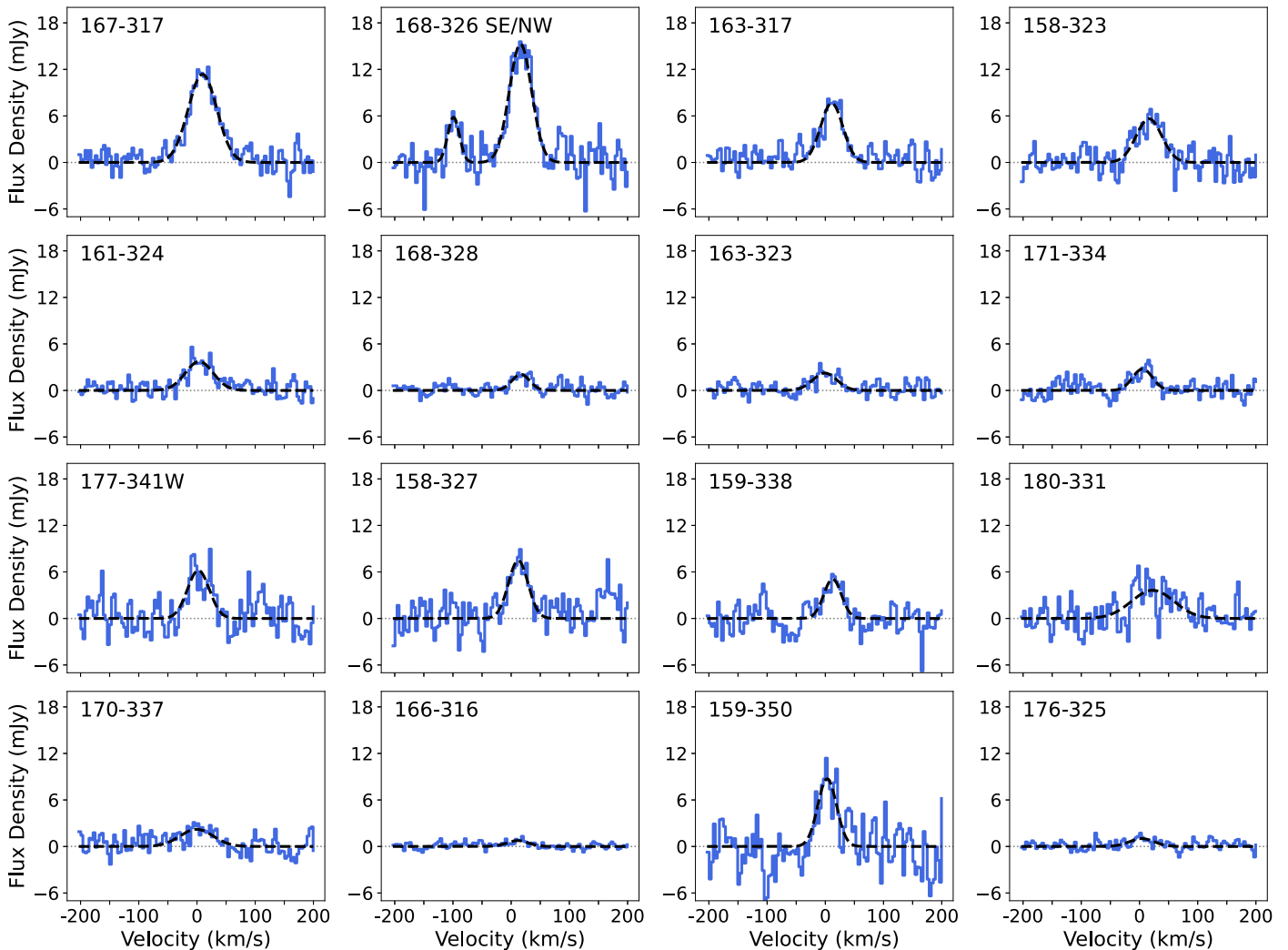
Figure 4. Radio recombination line spectra for H41α-detected proplyds, extracted from our data cube with 3.5 km s^{-1} channels. The spectra are centered about the rest frequency of the H41α line and constructed using circular apertures with diameters listed in Table 1. Solid blue lines show the computed spectra. Dashed black lines show best-fit Gaussian line profiles. Dotted gray lines show the zero points of the spectra. For 168–326 SE/NW, we fit two Gaussians in order to reproduce the detected He41α line at $v \approx -100$ km s^{-1}. Zoomed-in spectra for proplyds 168–328, 163–323, 166–316, and 176–325 are provided in Appendix B.

channels that are away from the line centers and where the line profiles differ most strongly, the signal-to-noise ratio is the lowest. We therefore opt to use Gaussian fitting to measure line properties, but note that higher sensitivity and spectral resolution are needed to firmly identify any non-Gaussian features (for a discussion on line broadening, see Section 4.1).

3.4. Electron Temperatures

Radio recombination lines are powerful tools for measuring the temperature of ionized gas. At millimeter and centimeter wavelengths, the excitation conditions of hydrogen recombination lines are dominated by collisions with ionized plasma (M. A. Gordon & R. L. Sorochenko 2009; B. T. Draine 2011). The emerging line intensities relate directly to the electron gas temperature via the Boltzmann equation, and the system is well approximated by local thermodynamic equilibrium (LTE).

Here, we use measurements of H41α emission and 3.1 mm free–free emission to calculate the electron temperature of each H41α-detected proplyd. As discussed in Appendix A

of K. L. Emig et al. (2020), the integrated line flux of an $n > 40$ hydrogen recombination line with $\Delta n = 1$ can be expressed as

$$\int S_n dv = (65.13 \text{ mJy km s}^{-1}) b_{n+1} \left(\frac{n_e n_p V}{5 \times 10^8 \text{ cm}^{-6} \text{ pc}^3} \right)$$

$$\times \left(\frac{D}{3.8 \text{ Mpc}} \right)^{-2} \left(\frac{T_e}{10^4 \text{ K}} \right)^{-1.5} \left(\frac{\nu}{100 \text{ GHz}} \right), \qquad (1)$$

where $\int S_n dv$ denotes the integrated line flux of a hydrogen radio recombination line transition to quantum number n, b_{n+1} is the non-LTE departure coefficient (for LTE, $b_{n+1} = 1$), n_e is the electron density, n_p is the hydrogen gas density, V is the source volume, D is the source distance, T_e is the electron temperature, and ν is the rest frequency of the hydrogen recombination line. Moreover, in the optically thin regime (as expected for proplyd free–free emission at 3.1 mm; e.g., P. D. Sheehan et al. 2016; R. D. Boyden & J. A. Eisner
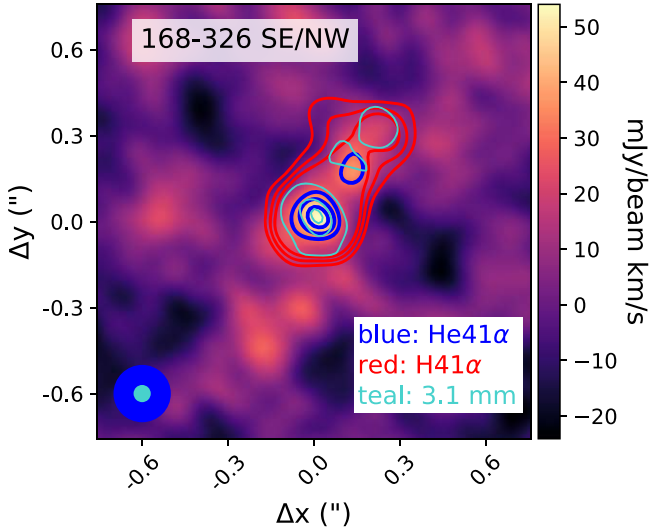
7

Figure 5. Moment 0 map of He41α for 168–326 SE/NW. This moment map is generated from velocity channels in the range -120 to -90 km s^{-1} with respect to the H41α rest frequency. Blue contours show 3.5σ, 4.5σ, and 5.5σ He41α emission. Teal contours show 3.1 mm continuum emission, with contours drawn at 10%, 50%, and 90% of the maximum continuum flux. Finally, red contours show 3.5σ, 4.5σ, and 5.5σ H41α emission (see, Figure 2). The synthesized beams for the 3.1 mm continuum (teal) and He41α (blue) images are shown in the lower left corner. The synthesized beam size is the same for the He41α and H41α moment 0 maps. All moment 0 maps are generated from our data cube with 10 km s^{-1} channels.

2024), the free–free flux density can be written as

$$S_{ff} = (2.080 \text{ mJy}) Z^{1.882} \left(\frac{n_e n_+ V}{5 \times 10^8 \text{ cm}^{-6} \text{ pc}^3} \right)$$
$$\times \left(\frac{D}{3.8 \text{ Mpc}} \right)^{-2} \left(\frac{T_e}{10^4 \text{ K}} \right)^{-0.323} \left(\frac{\nu}{100 \text{ GHz}} \right)^{-0.118}, \quad (2)$$

where S_{ff} is the free–free flux, n_+ is the density of ions, and $Z = 1$ is the effective nuclear charge.

Since $\int S_n dv$ and S_{ff} have similar dependencies on the electron density, volume, and source distance, their ratio is independent of these parameters. The ratio of $\int S_n dv$ over S_{ff} can therefore be expressed as

$$\frac{\int S_n dv}{S_{ff}} = (31.31 \text{ km s}^{-1}) b_{n+1} \left(\frac{T_e}{10^4 \text{ K}} \right)^{-1.177}$$
$$\times \left(\frac{n_p}{n_+} \right) \left(\frac{\nu}{100 \text{ GHz}} \right)^{1.118}. \quad (3)$$

If we assume that the emission region is composed primarily of ionized hydrogen and helium, then

$$\frac{n_p}{n_+} = \frac{n_{H^+}}{n_{H^+} + n_{He^+}} = (1 + n_{He^+}/n_{H^+})^{-1} = (1 + y^+)^{-1}, \quad (4)$$

where y^+ denotes the abundance of singly ionized helium relative to ionized hydrogen. Hence, we can derive the electron gas temperature via

$$T_e = (10^4 \text{ K}) \left[b_{n+1} (1 + y^+)^{-1} \right.$$
$$\left. \times \left(\frac{R_{LC}}{31.31 \text{ km s}^{-1}} \right)^{-1} \left(\frac{\nu}{100 \text{ GHz}} \right)^{1.118} \right]^{0.85}, \quad (5)$$

where $R_{LC} = \frac{\int S_n dv}{S_{ff}}$. For the remainder of this section, we refer to R_{LC} as the "line-to-continuum ratio."

Table 3 lists the 3.1 mm free–free fluxes used to compute the line-to-continuum ratios. To measure the free–free flux of each proplyd, we first compute a total 3.1 mm continuum flux over the same circular apertures used to construct the proplyd radio recombination line spectra (see Table 1). These apertures cover dust emission from the central disks in addition to free–free emission from ionized gas. To remove contributions from dust emission, we use the 3.1 mm dust continuum fluxes derived by N. P. Ballering et al. (2023) and N. P. Ballering et al. (2025, in preparation), as these were computed by spatio-spectrally isolating the central dust disk with combined 0.87 mm, 3.1 mm, 1.3 cm, 3.6 cm, and 6 cm ALMA and NSF's Karl G. Jansky Very Large Array (VLA) observations. The apertures used to measure dust continuum fluxes are comparable to the ones we use to derive continuum fluxes and radio recombination line spectra; we verified that small changes to the continuum apertures have a negligible effect on the derived 3.1 mm dust continuum fluxes. In Table 3, we list the derived dust continuum fluxes along with our 3.1 mm continuum and free–free fluxes.

To derive proplyd electron temperatures from the line-to-continuum ratios, we assume LTE, in which case $b_{n+1} = 1$. Our assumption of LTE is motivated by the departure coefficient calculations of K. L. Emig (2021), who find that, for $n > 40$, $b_{n+1} > 0.8$ for the expected electron densities and temperatures of proplyds in the ONC ($n_e > 10^5$ cm^{-3} and $T_e > 5000$ K; e.g., E. Churchwell et al. 1987; W. J. Henney et al. 2002; N. P. Ballering et al. 2023; see also Section 3.5). If we were to assume a somewhat lower departure coefficient (e.g., $b_{n+1} = 0.8$), the derived electron temperatures would be $\sim$1000–2000 K lower than our computed values.

For 168–326 SE/NW, we compute the electron temperature by taking y^+ as the ratio of the He41α and H41α line fluxes (see Table 2). Since hydrogen and helium radio recombination lines are optically thin (M. A. Gordon & R. L. Sorochenko 2009; B. T. Draine 2011), their line ratios provide a direct measurement of y^+. For all other H41α-detected proplyds, we assume $y^+ = 0.1$, which is consistent with the typical values measured in Galactic H II regions (e.g., E. Churchwell et al. 1974), including the Orion Nebula (e.g., J. A. Baldwin et al. 1991; C. H. M. Pabst et al. 2024). If we were to assume a somewhat larger helium abundance that is similar to what we infer for 168–326 SE/NW (e.g., $y^+ = 0.2$), the derived electron temperatures would decrease by $\sim$500–800 K (for a discussion on helium abundance, see Section 4.4).

Figure 6 plots the derived proplyd electron temperatures as a function of projected separation from θ^1 Ori C. In Table 3, we provide the derived electron temperatures and line-to-continuum ratios along with their uncertainties. The line-to-continuum ratios and electron temperatures are similar across our sample of H41α-detected proplyds, indicating that ionized gas from proplyds has a similar temperature over a range of disk, stellar, and environmental properties. Typically, we derive electron temperatures of $\sim$7000–9000 K. These are broadly consistent with the expected electron temperatures of solar-metallicity H II regions (e.g., T. J. Haworth et al. 2015; T. V. Wenger et al. 2019; D. S. Balser & T. V. Wenger 2024). However, they suggest that many proplyds have clumpy gas structures or have lower ionization front temperatures than the nominally assumed 10,000 K value for externally EUV-ionized photoevaporative winds (e.g., D. Johnstone et al. 1998).

Table 2
Measured He41α Properties for 168–326 SE/NW

Amp$_{\mathrm{He41\alpha}}$ (mJy) (1)	$V_{\mathrm{cen,He41\alpha'}}$ (km s^{-1}) (2)	$V_{\mathrm{cen,He41\alpha}}$ (km s^{-1}) (3)	FWHM$_{\mathrm{He41\alpha}}$ (km s^{-1}) (4)	$\int S_{\mathrm{He41\alpha}}\, dV$ (mJy km s^{-1}) (5)	y^+ (6)
5.82 ± 1.17	−98.94 ± 2.34	23.06 ± 2.34	23.71 ± 5.52	147 ± 17	0.200 ± 0.023

Notes. Column (1): best-fit He41α peak line flux. Column (2): best-fit He41α central velocity with respect to the H41α rest frequency. Column (3): best-fit He41α central velocity with respect to the He41α rest frequency. Column (4): best-fit He41α line width, computed as the Gaussian full width at half maximum. Column (5): integrated He41α line flux, derived by integrating over the best-fit Gaussian line profiles. Column (6): abundance of singly ionized helium relative to ionized hydrogen, computed as the ratio of the measured He41α and H41α line fluxes.

Table 3
Derived Proplyd Properties Based on Measurements of 3.1 mm Free–Free Emission and H41α Emission

ID (1)	$F_{\mathrm{cont,3.1\ mm}}$ (mJy) (2)	$F_{\mathrm{dust,3.1\ mm}}$ (mJy) (3)	$F_{\mathrm{ff,3.1\ mm}}$ (mJy) (4)	R_{LC} (km s^{-1}) (5)	r_{IF} (au) (6)	T_e (K) (7)	n_e (×10^6 cm^{-3}) (8)
167–317	23.39 ± 0.04	5.13 ± 2.85	18.26 ± 2.85	39 ± 7	32.5 ± 2.3	7100 ± 1100	12.62 ± 2.18
168–326 SE/NW	21.69 ± 0.03	2.40 ± 2.00	19.29 ± 2.01	38 ± 5	20.0 ± 1.2	6600 ± 800	16.33 ± 2.24
163–317	12.02 ± 0.04	2.93 ± 1.40	9.09 ± 1.40	40 ± 8	23.0 ± 0.1	6900 ± 1100	13.60 ± 2.50
158–323	13.00 ± 0.03	3.55 ± 1.52	9.45 ± 1.52	33 ± 7	27.3 ± 0.2	8200 ± 1500	11.87 ± 2.53
161–324	7.17 ± 0.03	2.18 ± 0.80	4.99 ± 0.80	45 ± 10	19.7 ± 0.1	6300 ± 1200	13.19 ± 2.83
168–328	4.70 ± 0.03	1.53 ± 0.55	3.17 ± 0.56	25 ± 7	19.1 ± 0.1	10,300 ± 2400	12.75 ± 3.35
163–323	6.09 ± 0.04	3.03 ± 0.71	3.06 ± 0.71	38 ± 13	16.4 ± 0.1	7200 ± 2000	17.57 ± 5.52
171–334	5.19 ± 0.02	1.61 ± 0.62	3.57 ± 0.62	33 ± 9	25.0 ± 0.3	8100 ± 2000	7.05 ± 1.92
177–341W	13.40 ± 0.02	1.89 ± 0.22	11.51 ± 0.22	25 ± 6	124.0 ± 0.4	10,200 ± 1900	2.69 ± 0.58
158–327	10.82 ± 0.03	0.97 ± 0.12	9.85 ± 0.13	32 ± 6	88.0 ± 0.4	8400 ± 1200	2.45 ± 0.42
159–338	3.22 ± 0.02	1.08 ± 0.32	2.14 ± 0.32	90 ± 23	25.6 ± 0.5	3500 ± 800	4.34 ± 1.06
180–331	6.71 ± 0.02	0.80 ± 0.10	5.91 ± 0.11	56 ± 11	88.0 ± 0.4	5200 ± 900	2.34 ± 0.44
170–337	9.04 ± 0.02	1.99 ± 0.24	7.04 ± 0.24	23 ± 6	88.0 ± 0.4	11,200 ± 2500	4.18 ± 1.05
166–316	2.44 ± 0.04	0.87 ± 0.31	1.57 ± 0.32	22 ± 8	17.3 ± 0.2	11,400 ± 3500	10.26 ± 3.57
159–350	26.86 ± 0.03	11.92 ± 1.34	14.94 ± 1.34	24 ± 5	144.0 ± 0.4	10,800 ± 2100	2.44 ± 0.53
176–325	4.44 ± 0.01	1.79 ± 0.77	2.65 ± 0.77	20 ± 8	29.4 ± 0.4	12,300 ± 4300	6.36 ± 2.50

Notes. Column (1): proplyd name. Column (2): 3.1 mm continuum flux density, computed over the same source aperture listed in Table 1. Column (3): 3.1 mm dust continuum flux density, taken from N. P. Ballering et al. (2023) and N. P. Ballering et al. (2025, in preparation). Column (4): free–free flux density at 3.1 mm, computed as the difference between the 3.1 mm total continuum flux and 3.1 mm dust continuum flux. Column (5): ratio of the integrated H41α line flux and 3.1 mm free–free flux. Column (6): ionization front radius. For proplyds 177–341W, 158–327, 180–331, 170–337, and 159–350, we list the ionization front radii derived previously by N. P. Ballering et al. (2023). For all other sources, the ionization front radius is measured by fitting elliptical Gaussians to the high-resolution 3.1 mm continuum subimages of each source (see Appendix A), where the ionization front radius is taken as the best-fit half-width-at-half-maximum minor axis. For 168–326 SE/NW, the provided ionization front radius is the average of the values obtained for 168–326 SE and 168–326 NW. Column (7): electron gas temperature, derived from Equation (5). Column (8): electron density, derived from Equation (6).

3.5. Electron Densities

Our ability to measure electron temperatures with radio recombination lines allows for a more accurate constraint of proplyd electron densities. For each H41α-detected proplyd in our sample, we compute a free–free optical depth from the peak 3.1 mm free–free flux density via $\tau_{ff} = I_\nu / B_\nu(T_e)$, where I_ν denotes the peak intensity and B_ν denotes the Planck function. We then convert the free–free optical depth into an electron density under the assumption that the ionized gas is concentrated in a thin hemispherical shell at the ionization front. As shown in N. P. Ballering et al. (2023), this assumption yields the equation

$$n_e = \left(\frac{\mathrm{EM}^2 \sigma}{8 R_{\mathrm{IF}}} \right)^{1/3}, \qquad (6)$$

where $\sigma = 6.3 \times 10^{-18}\ \mathrm{cm}^2$ is the ionization cross section; R_{IF} is the radius at the proplyd ionization front; and EM is the emission measure, which relates directly to the free–free optical depth via Equation (A.1b) of P. G. Mezger & A. P. Henderson (1967):

$$\left(\frac{\mathrm{EM}}{\mathrm{pc\ cm}^{-6}} \right) = \left(\frac{\tau_{ff}}{3.28 \times 10^{-7}} \right) \left(\frac{T_e}{10^4\ \mathrm{K}} \right)^{1.35} \left(\frac{\nu}{\mathrm{GHz}} \right)^{2.1}. \qquad (7)$$

We note that, if the emitting gas layer is thicker than we have assumed (see W. J. Henney & S. J. Arthur 1998; W. J. Henney & C. R. O'Dell 1999), then the inferred electron densities would be ~5–10 times lower than the values derived from a thin hemispherical shell geometry (see discussion in R. D. Boyden & J. A. Eisner 2024). Our current free–free-based electron densities may thus be upper limits that have been more robustly pinpointed with direct measurements of electron temperature.

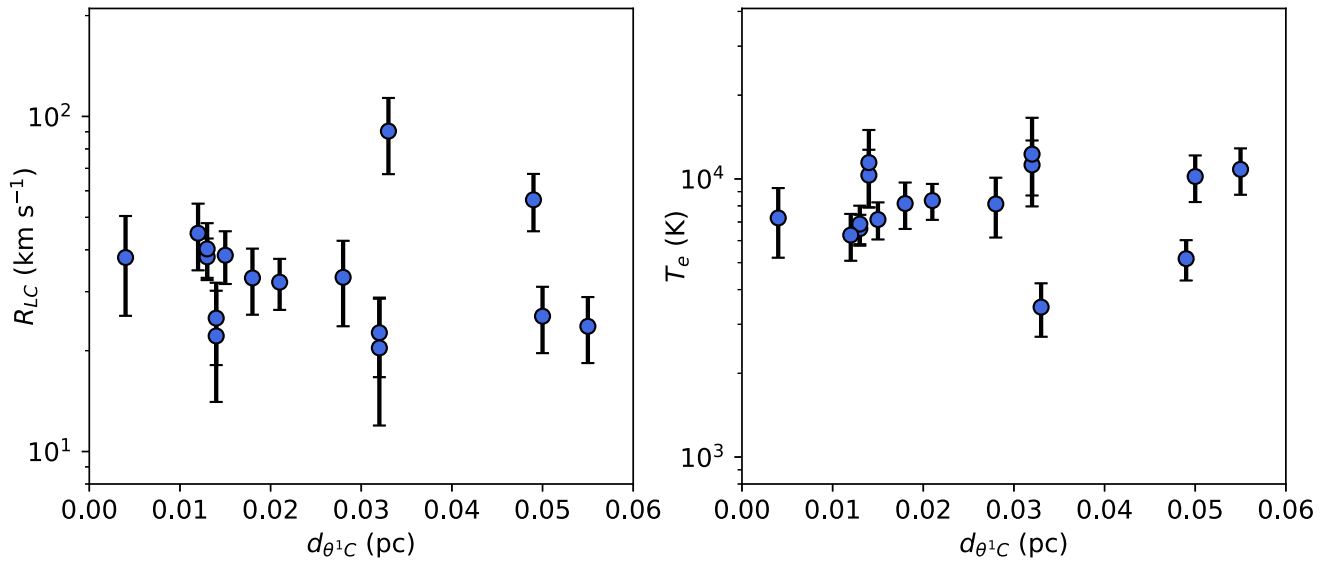For the five H41α-detected proplyds whose disks and ionization fronts are spatially isolated in the 3.1 mm

Figure 6. Left: ratio of integrated H41α line flux to 3.1 mm free–free continuum flux for H41α-detected proplyds, plotted as a function of projection separation from θ^1 Ori C. Right: proplyd electron gas temperature, derived from Equation (5), as a function of projected separation from θ^1 Ori C.

continuum, we use the ionization front radii from N. P. Ballering et al. (2023) to compute the electron density. These ionization front radii were computed by taking surface brightness cuts along the direction in which the disks and ionization fronts were detected and spatially isolated. For the compact proplyds whose 3.1 mm morphologies are dominated by the ionization front, we measure their ionization front radii by fitting elliptical Gaussians to the high-resolution 3.1 mm subimages shown in Appendix A, where we take the best-fit half-width-at-half-maximum minor axis as the ionization front radius. Combining the measured ionization front radii with the measured 3.1 mm free–free fluxes and electron temperatures in Table 3, we derive electron densities of $\sim 10^6$–10^7 cm^{-3}. In Table 3, we list the computed ionization front radii and electron densities of each proplyd.

Figure 7 plots the ionization front radii and electron densities of each H41α-detected proplyd as a function of projected separation from θ^1 Ori C. We identify a positive correlation between ionization front radius and projected separation (consistent with previous studies; e.g., N. P. Ballering et al. 2023; M.-L. Aru et al. 2024). We also identify, for the first time, a negative correlation between electron density and projected separation. Both correlations remain when we restrict our fitting to the compact proplyds whose ionization front radii are measured from Gaussian fitting (i.e., when we exclude proplyds whose ionization front radii were measured with surface brightness cuts). Both trends can be explained by a reduction in EUV flux at increased projected separations, which enables photoevaporating gas to expand further away from the disk before becoming externally ionized (D. Johnstone et al. 1998). One proplyd, 158–327, has a lower electron density and a larger ionization front radius in comparison with other proplyds at similar projected separations. This suggests that 158–327 is farther from θ^1 Ori C than what is implied by its projected separation, or that trends with projected separation break down with increased sample sizes (e.g., R. J. Parker et al. 2021a).

4. Discussion

4.1. Line Widths

The H41α line widths that we derive for our sample of ONC proplyds are systematically larger than the line widths expected from pressure, thermal, and turbulent broadening. For an H II region, the line width of a radio recombination line can be written as

$$\Delta v_{\mathrm{RRL}} = 0.5343 \Delta v_p + [(\Delta v_t)^2 + (\Delta v_d)^2 + (0.4657 \Delta v_p)^2]^{1/2} \tag{8}$$

(E. Keto et al. 2008). Here, Δv_{RRL} denotes the overall line width of a radio recombination line. Δv_p denotes the Lorentzian width due to pressure broadening, which scales with the electron density, electron temperature, and principal quantum number as

$$\Delta v_p = (1.43 \times 10^{-5} \, \mathrm{km \, s^{-1}}) \left(\frac{n}{100} \right)^{7.4} \left(\frac{10^4 \, \mathrm{K}}{T_e} \right)^{0.1}$$
$$\times \left(\frac{n_e}{10^4 \, \mathrm{cm^{-3}}} \right) \left(\frac{c}{\mathrm{km \, s^{-1}}} \right), \tag{9}$$

where c denotes the speed of light (M. Brocklehurst & M. J. Seaton 1972). Δv_t denotes the Gaussian width due to thermal broadening, which, for a hydrogen recombination lines, scales with the electron temperature as

$$\Delta v_t = \sqrt{\frac{8 \ln 2 \, k_b T_e}{m_p}}, \tag{10}$$

where k_b is the Boltzmann constant and m_p is the proton mass. Finally, Δv_d denotes the Gaussian width due to dynamical broadening from turbulence and/or ordered gas motions.

Figure 8 plots the inferred thermal and pressure line widths for each proplyd, computed via Equations (9) and (10) using the electron densities and temperatures listed in Table 3. Combining these with the measured H41α line widths in
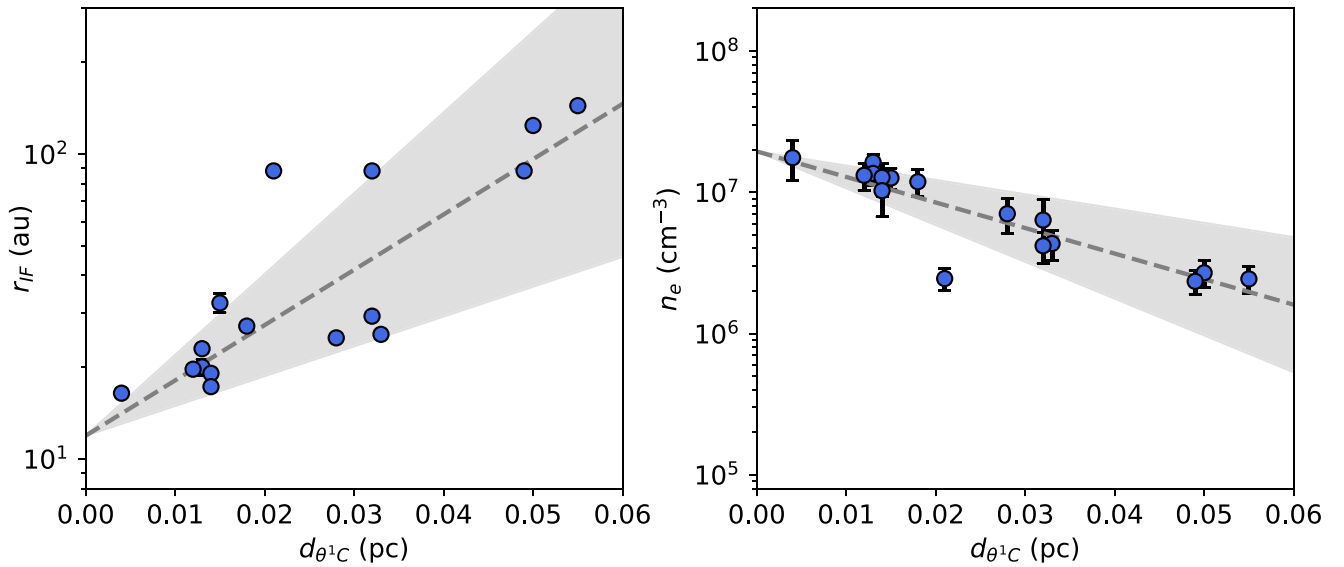
Figure 7. Left: proplyd ionization front radius as a function of projection separation from θ^1 Ori C. The fitted trend to the data is $\log_{10}(r_{IF}/AU) = (1.076 \pm 0.004) + (18.135 \pm 8.362)(d_{toc}/pc)$. Right: proplyd electron density, derived from Equation (6), as a function of projected separation from θ^1 Ori C. The fitted trend to the data is $\log_{10}(n_e/cm^{-3}) = (7.289 \pm 0.007) + (-18.081 \pm 7.962)(d_{toc}/pc)$.
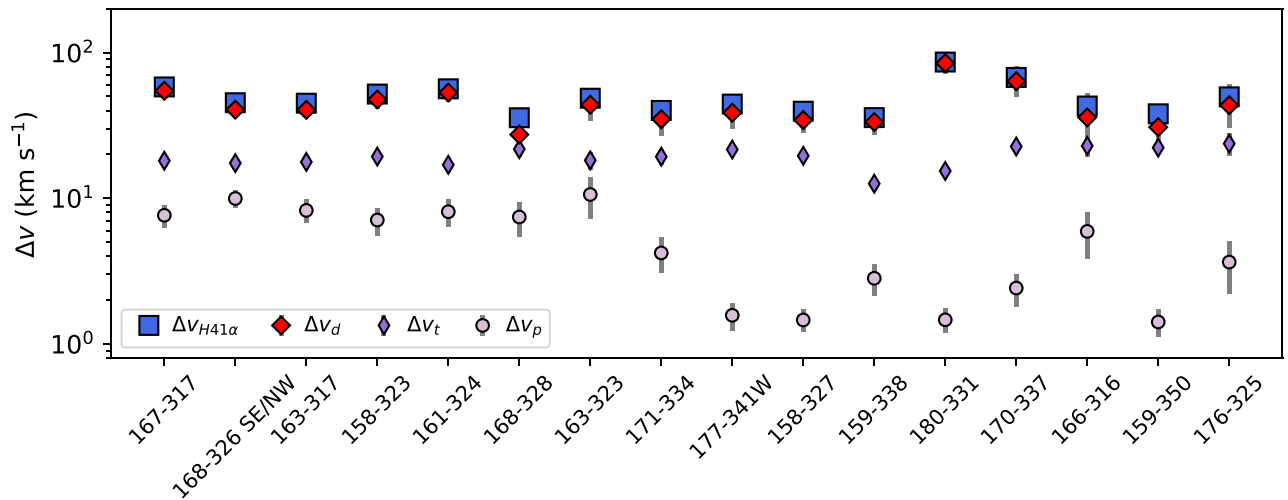

Figure 8. Measured H41α line width ($\Delta v_{H41\alpha}$) of each proplyd plotted along with the inferred line widths due to thermal broadening (Δv_t), pressure broadening (Δv_p), and dynamical broadening (Δv_d).

Table 1, we derive a dynamical line width, Δv_d, for each proplyd via Equation (8), and we show these in Figure 8 along with the measured H41α line widths and inferred thermal and pressure line widths.

The line widths expected from pressure broadening are too low ($\sim$1–10 km s^{-1}) to dominate the overall line broadening. Considering that our 3.1 mm continuum observations have detected the brightest and thus highest-electron-density ($n_e \approx 10^6$–10^7 cm^{-3}) proplyds in the ONC, it seems unlikely that any ONC proplyds are dense enough for pressure broadening to dominate the broadening of $n < 50$ recombination lines, though it may contribute for the highest-density proplyds. Moreover, while the thermal line widths ($\sim$20–25 km s^{-1}) are broader than the line widths expected from pressure broadening, they are typically much lower than the measured H41α line widths.

Figure 8 demonstrates that dynamical broadening provides the greatest contribution to the measured H41α line widths. In

all cases, the inferred dynamical line widths are within 1σ of the measured H41α line widths. And, in the majority of cases, the dynamical widths exceed the thermal and pressure line widths by $>2\sigma$. Since these dynamical widths are broader than the line widths expected from turbulence in H II regions ($\sim$15 km s^{-1}; e.g., L. D. Anderson et al. 2011; C. H. M. Pabst et al. 2024), we conclude that the dynamical and thus overall line broadening of proplyd H41α emission is dominated by outflowing gas motions, consistent with the presence of velocity gradients in Figure 3.

The broad H41α line widths of proplyds can be explained by an ionized photoevaporative wind. As gas photoevaporates off the disk and passes through an ionization front, pressure gradients cause the flow to accelerate from initial velocities of 1–3 km s^{-1} to supersonic values as high as $\sim$30–60 km s^{-1} (for illustrative examples, see S. Richling & H. W. Yorke 2000). These expected terminal velocities match up well with the H41α line widths measured in our sample.

Another possibility is that the broad H41α line widths could be attributed to emission from both a disk wind and a jet. Stellar winds and jets associated with accretion tend to launch material at higher velocities than disk winds (G. Anglada et al. 2018, and references therein). In high-mass protostars, jets produce the bulk of the hydrogen recombination line emission at high systemic velocities, though it is typically fainter than the disk emission seen at lower velocities. (e.g., S. Prasad et al. 2023; A. Martínez-Henares et al. 2024). Two of the broadest-line-width proplyds in our sample—167–317 and 170–337— are known jet hosts (J. Bally et al. 1998; W. J. Henney et al. 2002; Y. G. Tsamis & J. R. Walsh 2011; J. E. Méndez-Delgado et al. 2021). Moreover, 180–331 has a measured H41α line width that exceeds the typical $\sim$30–60 km s^{-1} velocities expected from external photoevaporation alone (see Table 1). It seems plausible that the H41α line profile of 180–331 is contaminated with high-velocity jet emission that, at our current sensitivity and resolution, cannot be distinguished from the photoevaporative wind. With deeper, higher-resolution radio recombination line observations, we can isolate disk wind versus jet emission while also taking census of jet-hosting proplyds in the ONC, as demonstrated in studies of high-mass protostars (e.g., S. J. D. Purser et al. 2016; I. Jiménez-Serra et al. 2020; L. Moscadelli et al. 2021; R. Galván-Madrid et al. 2023; S. Prasad et al. 2023; A. Martínez-Henares et al. 2024).

Regardless of whether the H41α line widths are driven solely by disk winds or by disk winds and jets, our observations reveal that hydrogen radio recombination lines offer a new roadmap for measuring the kinematics—and by extension, the mass-loss rates—of ionized externally photoevaporating disks. Higher angular resolution observations will enable mapping of the flow geometry and velocity along different positions of the proplyd, allowing for more accurate determinations of the mass-loss rates, rotational broadening, and gas acceleration mechanisms. Millimeter- and submillimeter-band recombination lines appear especially suitable for mapping proplyd kinematics. At longer wavelengths, pressure broadening becomes significant, to the point where, even for low-density photoevaporative flows, the line widths of recombination lines are dominated by pressure broadening (see Equation (9)). In future work, we intend to develop a framework for measuring the mass-loss rates of proplyds with radio recombination lines.

4.2. Radio Recombination Lines as Thermometers for Photoevaporative Winds

Our analysis demonstrates that hydrogen radio recombination lines provide a straightforward way to measure the temperatures of proplyd ionization fronts. At optical wavelengths, which have thus far been used to derive proplyd electron temperatures (e.g., Y. G. Tsamis et al. 2011, 2013; A. Mesa-Delgado et al. 2012), non-LTE effects dominate the gas excitation, and the electron densities and temperatures cannot be derived independently. Nebular background, saturation, and reddening effects also introduce large systematic uncertainty to optical-based measurements of electron temperature, though in the case of proplyds, empirical correction techniques have been developed to mitigate these uncertainties (e.g., W. J. Henney & C. R. O'Dell 1999; Y. G. Tsamis et al. 2011; A. Mesa-Delgado et al. 2012).

With radio recombination lines, we can derive density-independent measurements of electron temperature that are unaffected by reddening, saturation, or the nebular background. By detecting hydrogen and helium radio recombination lines from proplyds, we can also constrain ionized helium abundances to allow for a more robust determination of the electron temperature (see Equation (5)).

Radio-recombination-line-based measurements of electron temperature are likely to achieve high precision when carried out at wavelengths longer than 3.1 mm, in particular for compact proplyds where it is challenging to spatially separate the disk and ionization front. Currently, the precision on our derived electron temperatures is limited by the uncertainties on the 3.1 mm free–free fluxes, which are higher than the nominal continuum rms due to the spectral decomposition employed to separate out dust and free–free emission. Dust emission has a positive spectral index (R. H. Hildebrand 1983), and at wavelengths between $\sim$7 and 20 mm, proplyd continuum flux measurements are expected to be dominated by optically thin free–free emission from the ionized wind (e.g., R. K. Mann et al. 2014; P. D. Sheehan et al. 2016; R. D. Boyden & J. A. Eisner 2024). At these long wavelengths, hydrogen recombination lines remain in LTE down to densities as low as $\sim$10^2 cm^{-3} and temperatures as low as $\sim$1000 K (B. T. Draine 2011; K. L. Emig 2021). Long millimeter- and centimeter-based measurements of electron temperature should therefore be even more robust against systematic uncertainties associated with non-LTE effects.

By obtaining accurate, high-precision electron temperatures with radio recombination lines, we can more accurately measure the densities (e.g., see Section 3.5), chemical abundances, and mass-loss rates of ionized photoevaporative winds. All of these quantities depend on the assumed electron temperature, with the chemical abundances derived from optical forbidden lines being especially sensitive to the electron temperature (e.g., A. Mesa-Delgado et al. 2012; J. E. Méndez-Delgado et al. 2023).

4.3. Properties of H41α Nondetections

We perform a stacking analysis to explore the properties of ONC disks not detected in H41α. The left panel of Figure 9 shows the 3.1 mm free–free fluxes of all mm-detected ONC disks in our maps as a function of projected separation from θ^1 Ori C. The right panel shows stacked average radio recombination line spectra for the H41α nondetections. We compute the free–free fluxes and spectra of H41α nondetections by following the same procedures used for the H41α detections, except here we adopt a uniform circular aperture diameter of 0″5. Since the H41α-detected proplyds tend to be free–free luminous and close to θ^1 Ori C (see Figure 9), we generate two stacked spectra, one for all $\sim$200 H41α nondetections, and another for the subset of nondetections with free–free fluxes and projected separations similar to those of the H41α detections (i.e., $S_{ff} > 1.5$ mJy and $d_{toc} < 0.06$ pc; see Figure 9).

When we restrict our stacking to the 10 nondetections with free–free fluxes and projections separations similar to those of the H41α detections, we see a $\sim$4σ detection of H41α in the stacked spectrum. The H41α emission of these sources appears to have just fallen below our detection threshold. Since free–free-bright H41α nondetections likely have electron densities similar to those of the H41α detections, we expect an H41α nondetection to, in this case, be attributed to either smaller line-to-continuum ratios or increased noise levels. We have
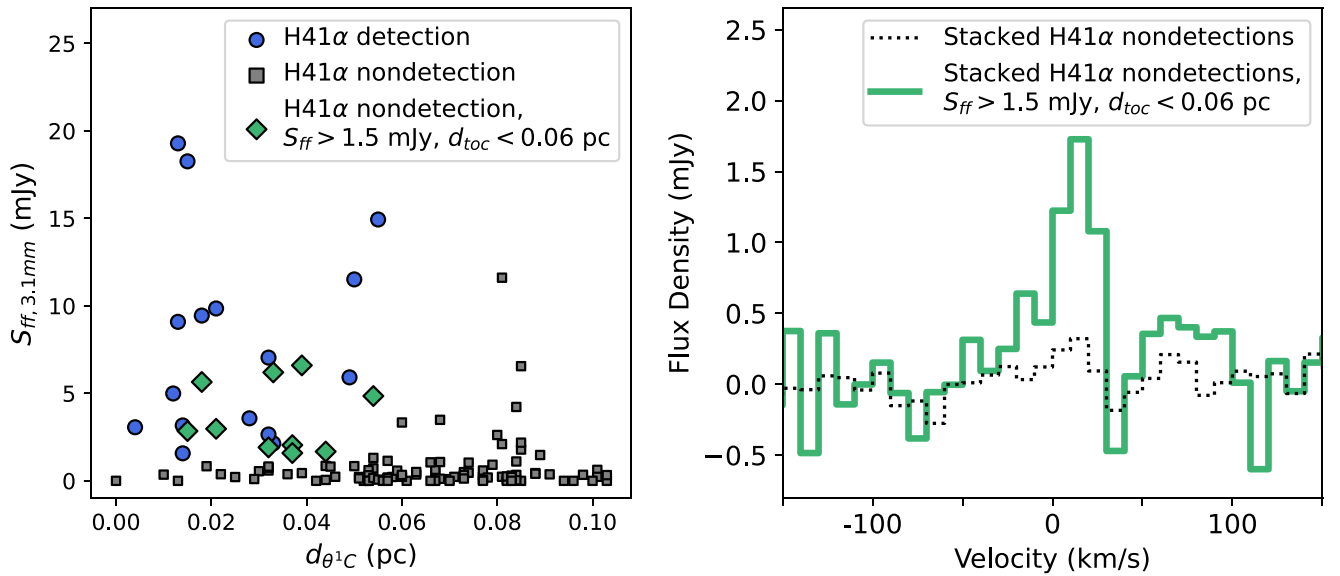
Figure 9. Left: 3.1 mm free–free fluxes of ONC disks (N. P. Ballering et al. 2023), plotted as a function of projection separation from θ^1 Ori C. Blue circles indicate H41α-detected proplyds. Green diamonds indicate H41α nondetections with 3.1 mm free–free fluxes >1.5 mJy and projected separations <0.06 pc (i.e., with free–free fluxes and projected separations similar to those of the H41α detections; see Tables 1 and 3). Gray squares indicate all other H41α nondetections. Right: stacked average spectra for all H41α nondetections (dotted black line) and for the subset of H41α nondetections with 3.1 mm free–free fluxes >1.5 mJy and projected separations <0.06 pc (solid green line). The stacked spectra are constructed using our data cube with 10 km s^{-1} channels.

examined the noise fluctuations in our ALMA data cube to check whether the rms noise is higher toward the positions of free–free-bright H41α nondetections versus H41α detections. We find no significant differences in the local rms, indicating that free–free-bright H41α nondetections are driven by lower line-to-continuum ratios—and by extension, warmer electron temperatures and/or lower gas metallicities (see Equation (3)).

When we stack all $\sim$200 continuum sources in our maps, we see no H41α detection in the stacked spectrum, stacked moment maps, or stacked channel maps. This suggests that the average ONC disk has an H41α line flux that is $\geqslant$10 times fainter than our current rms noise levels (i.e., <0.5 mJy). For most disks, we expect this to be due to a lack of an ionization front, since only $\sim$50% of mm-detected ONC disks are HST-identified proplyds (e.g., J. A. Eisner et al. 2018). But in cases where an H41α nondetection is a known proplyd with a fainter free–free flux than that of an H41α-detected proplyd, we expect a factor of $\sim$10 lower H41α line flux to be attributed to a combination of warmer gas temperatures, lower gas metallicities, and/or lower electron densities (see Equations (1) and (3)).

Equation (1) suggests that a factor of $\sim$3 reduction in density reduces the H41α line intensity by a factor of $\sim$10. The majority of ONC proplyds may therefore have electron densities that are $\sim$3 times lower than the minimum electron density in our H41α-detected proplyd sample, which would imply electron densities of <10^6 cm^{-3} (see Table 3). Moreover, if the electron density correlates inversely with distance from θ^1 Ori C, as suggested by Figure 7, this would imply that the majority of proplyds not detected in H41α are farther from θ^1 Ori C than what is implied by their projected separations.

Our stacking analysis indicates that the ONC contains a large population of proplyds with different physical conditions than the ones detected in this paper. Deeper radio recombination line observations are needed to determine whether it is the electron density, electron temperature, or gas metallicity that varies the most across photoevaporative disk winds in the ONC.

4.4. Helium Abundances

Previous studies have used hydrogen and helium radio recombination lines to measure y^+, the abundance of singly ionized helium relative to ionized hydrogen, in H II regions (e.g., E. Churchwell et al. 1974; P. A. Shaver et al. 1983; M. Peimbert et al. 1988; G. Garay et al. 1998; D. A. Roshi et al. 2017; C. H. M. Pabst et al. 2024). Values of y^+ that exceed 0.08 are thought to arise from the enrichment of interstellar matter via galaxy evolution, since Big Bang nucleosynthesis suggests a primordial helium abundance of 0.08 for the Universe (E. Churchwell et al. 1974). Values below 0.08 indicate that the helium gas is not fully ionized, which can occur when an H II region is excited by stars that do not emit intense levels of helium-ionizing ($\gtrsim$24 eV) radiation (i.e., spectral types later than $\sim$O6), when dust in the H II region preferentially absorbs helium-ionizing photons, or when non-LTE and/or opacity effects become significant (see discussion in E. Churchwell et al. 1974; G. Garay et al. 1998). When the helium and hydrogen gas are fully ionized, y^+ provides a direct measurement of the overall helium abundance (E. Churchwell et al. 1974).

The detection of H41α and He41α toward 168–326 SE/NW enables us to constrain the helium abundances of protoplanetary disks with radio recombination lines. As shown in Table 2, we find that the He41α to H41α line ratio of 168–326 SE/NW implies a singly ionized helium abundance of $\sim$0.2. This is somewhat larger than the typical helium abundances measured in H II regions (E. Churchwell et al. 1974). It is also larger than the expected helium abundance of the Orion Nebula, for which optical- and radio-recombination-line-based studies find values of $\sim$0.1 (e.g., J. A. Baldwin et al. 1991; C. H. M. Pabst et al. 2024).

The enhanced helium abundance of 168–326 SE/NW may be driven by this system's proximity to θ^1 Ori C. Typically, the helium abundance of the Orion Nebula is measured from observations targeting ionized gas that is $\gtrsim$0.05 pc from θ^1 Ori C (e.g., J. A. Baldwin et al. 1991; C. H. M. Pabst et al. 2024).
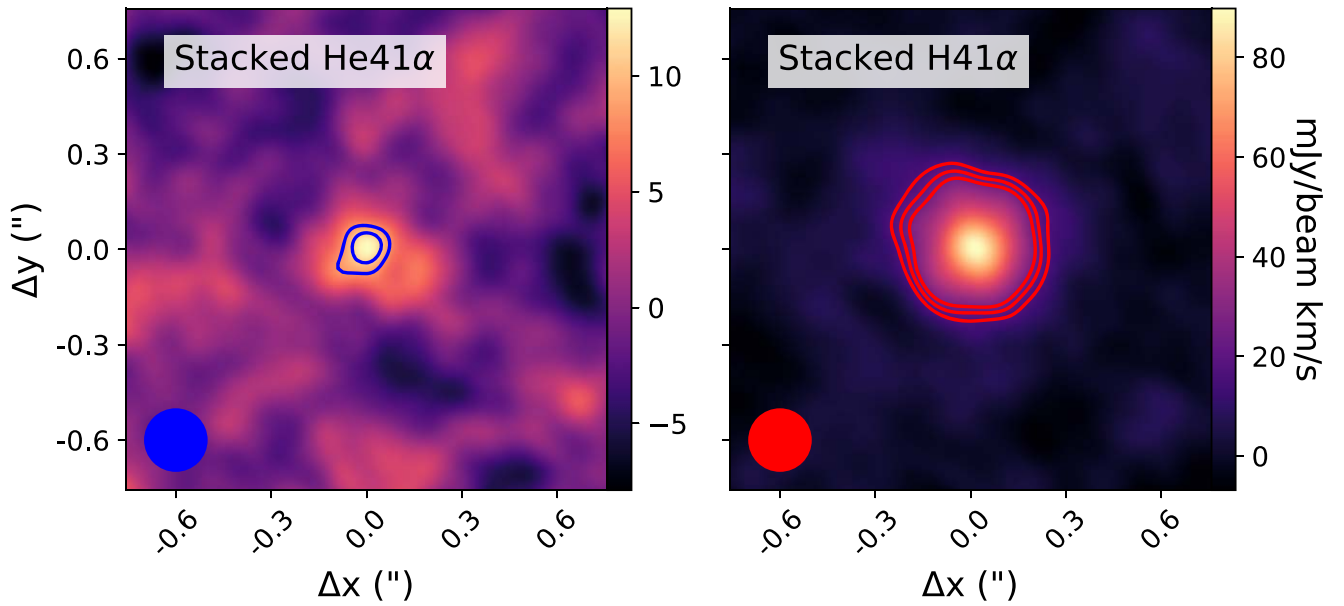
Figure 10. Stacked He41α moment 0 map (left panel) and H41α moment 0 map (right panel) for all H41α-detected proplyds not detected in He41α. All stacked He41α moment 0 maps are generated from velocity channels in the range −120 to −90 km s^{-1} with respect to the H41α rest frequency, while all stacked H41α moment 0 maps are generated from velocity channels in the range 0–60 km s^{-1} with respect to the H41α rest frequency. Contours show 3.5σ, 4.5σ, and 5.5σ emission. The synthesized beam is shown in the bottom left corner of each panel. Stacked moment 0 maps are generated from our data cube with 10 km s^{-1} channels.

168–326 SE/NW is ∼0.013 pc (in projected separation) from θ^1 Ori C (see Table 1), so it is likely exposed to stronger levels of helium-ionizing radiation and less affected by extinction than the gas at larger projected separations, in which case we might expect our derived helium abundance to be more reflective of the Orion Nebula's helium abundance.

Another possibility is that our helium abundance measurement is contaminated by line blending of helium and carbon recombination lines (e.g., E. Churchwell et al. 1974; M. Peimbert et al. 1988; C. H. M. Pabst et al. 2024). The C41α recombination line is about ∼8 MHz (∼30 km s^{-1}) from the He41α line, and if C41α emission from 168–326 SE/NW were to have a line width similar to that of the detected H41α emission, it would partially overlap with He41α. The relative line fluxes of carbon and helium radio recombination lines vary depending on the incident radiation field, but in H II regions excited by $\gtrsim$O6 stars, carbon radio combination lines are typically ∼5–10× fainter than helium radio recombination lines (for examples in the Orion Nebula, see C. H. M. Pabst et al. 2024). Line blending may therefore only have a modest (∼25%) effect on our helium abundance measurement for 168–326 SE/NW, but this needs to be confirmed with higher spectral resolution observations that isolate C41α and He41α emission.

An increased sample of proplyd helium abundance measurements, combined with deeper and higher angular observations that can more readily spatially isolate helium recombination lines from close-separation proplyds (i.e., 168–326 SE and 168–326 NW), could also help to determine whether proplyds are helium-rich relative to the Orion Nebula or whether the Orion Nebula is more helium-rich than currently thought. Figure 10 shows stacked average moment 0 maps of He41α and H41α for all H41α-detected proplyds that are not detected in He41α. We detect He41α at >4σ in the stacked moment 0 maps, indicating that deeper observations will detect helium radio recombination lines from additional proplyds. We compute an average singly ionized helium abundance for the

stacked sources by taking the ratio of the stacked He41α and H41α moment 0 emission. Depending on the chosen aperture, we find values of y^+ that range from ∼0.12 to 0.16. This suggests that the average H41α-detected proplyd is less abundant in ionized helium than 168–326 SE/NW. The helium ionization fraction of proplyds—and by extension, gas in the Orion Nebula—may therefore vary depending on projected separation from θ^1 Ori C.

Deeper observations may also detect radio recombination lines from oxygen and other heavy atoms. These lines have recently been detected in the Orion Nebula (e.g., X. Liu et al. 2023), and if hydrogen, helium, carbon, and oxygen radio recombination lines were to be detected toward proplyds, we would be able to measure the elemental abundances of photoevaporating disks with radio recombination lines. Since the most massive star in the ONC, θ^1 Ori C, has a spectral type of O6 (C. R. O'Dell et al. 2017), it is hot enough to emit the intense levels of hard (>10 eV) EUV photons needed to ionize hydrogen, helium, and heavier atoms. This in contrast with other proplyd-hosting clusters in Orion (e.g., NGC 1977 and NGC 2024; J. Bally et al. 2012; J. S. Kim et al. 2016; T. J. Haworth et al. 2021; R. D. Boyden & J. A. Eisner 2024), whose most massive stars have later spectral types and are less likely to be emitting significant levels of hard EUV radiation (e.g., A. Bik et al. 2003; D. E. Peterson & S. T. Megeath 2008).

5. Conclusions

We presented ALMA observations that produced the first detection of radio recombination lines from a protoplanetary disk. We mosaicked the central 2′.0 × 2′.5 of the ONC at 3.1 mm, and because the ALMA spectral setup covered the $n = 42$ to $n = 41$ transitions of hydrogen and helium, we were able to search for hydrogen and helium radio recombination lines toward the positions of >200 protoplanetary disks.

We detect H41α emission from 17 protoplanetary disks. The detections are all HST-identified proplyds within 0.06 pc (in projection separation) of the massive star θ^1 Ori C. For all

detections, we find that the H41α emission is associated with the locations of proplyd ionization fronts, indicating that the H41α line is tracing gas that has been externally photo-evaporated off the disks' surfaces. For a subset of detections, the H41α emission exhibits a near-linear velocity gradient that is consistent with the gradients expected from photoevaporative disk winds.

We measured the line fluxes and line widths of the detected H41α lines by fitting Gaussian line profiles to the observed spectra. The H41α-detected proplyds span a range of H41α line fluxes, but they typically have similar H41α line-to-continuum ratios. For most proplyds, the derived line-to-continuum ratios imply electron gas temperatures of $\sim$7000 to $\sim$9000 K and electron densities of $\sim$10^6 to $\sim$10^7 cm^{-3}. We find that proplyd electron density correlates inversely with projected separation from θ^1 Ori C, consistent with the behavior expected from a reduction in UV flux at increased projected separations. The derived electron temperatures, on the other hand, show no correlation with projected separation.

For the H41α line widths, we find typical full widths at half maximum of $\sim$40–60 km s^{-1}, which are significantly broader than the line widths expected from thermal, turbulent, and pressure broadening. We suggest that the broadening of proplyd H41α emission is dominated by outflowing gas motions associated with external photoevaporation, since line widths of $\sim$40–60 km s^{-1} match up well with the expected terminal velocities of photoevaporative disk winds that have passed through an ionization front. However, for the couple of proplyds with line widths >60 km s^{-1}, we suspect that the presence of externally ionized jets is also contributing to the overall line broadening.

Finally, we detect He41α emission from the H41α-detected source 168–326 SE/NW. We find that this system's He41α to H41α line ratio implies a helium abundance that is greater than the canonical helium abundance of the Orion Nebula. However, with our current observations, we cannot rule out the possibility that our helium abundance measurement is contaminated by line blending of carbon and helium recombination lines. Deeper, higher spectral resolution observations are needed to more reliably measure the helium abundances of proplyds. Our stacking analysis suggests that the helium ionization fraction of proplyds correlates with projected separation from θ^1 Ori C, but this needs to be confirmed with direct measurements.

Our study demonstrates that radio recombination lines are readily detectable in ionized externally photoevaporating disks. This essentially opens up a new way to measure disk properties in clustered (i.e., typical) star formation environments. Millimeter- and submillimeter-band recombination lines appear especially suitable for mapping the kinematics of photoevaporating disks, given that these lines are less likely to be affected by pressure broadening. Millimeter- and centimeter-band recombination lines appear suitable for measuring the densities, temperatures, and chemistry of proplyd ionization fronts, since these lines remain in LTE down to low gas densities and temperatures. In the immediate future, we intend to develop a framework for measuring the mass-loss rates of ionized photoevaporating disks with high angular resolution radio recombination line observations.

By measuring the physical conditions of large samples of photoevaporating disks with radio recombination lines, we will be able to gain new insights into how the radiation environments of stellar clusters shape the demographics of disks and exoplanets. When ALMA's Wideband Sensitivity Upgrade is completed, and when the next-generation Very Large Array is commissioned, we expect radio recombination line surveys of protoplanetary disks to become increasingly feasible over large disk samples.

Appendix A
Continuum Images

Here, we include Figure 11, which shows the 3.1 mm continuum subimages of each H41α-detected proplyd. These subimages are generated from the full high-resolution continuum mosaic of N. P. Ballering et al. (2023).
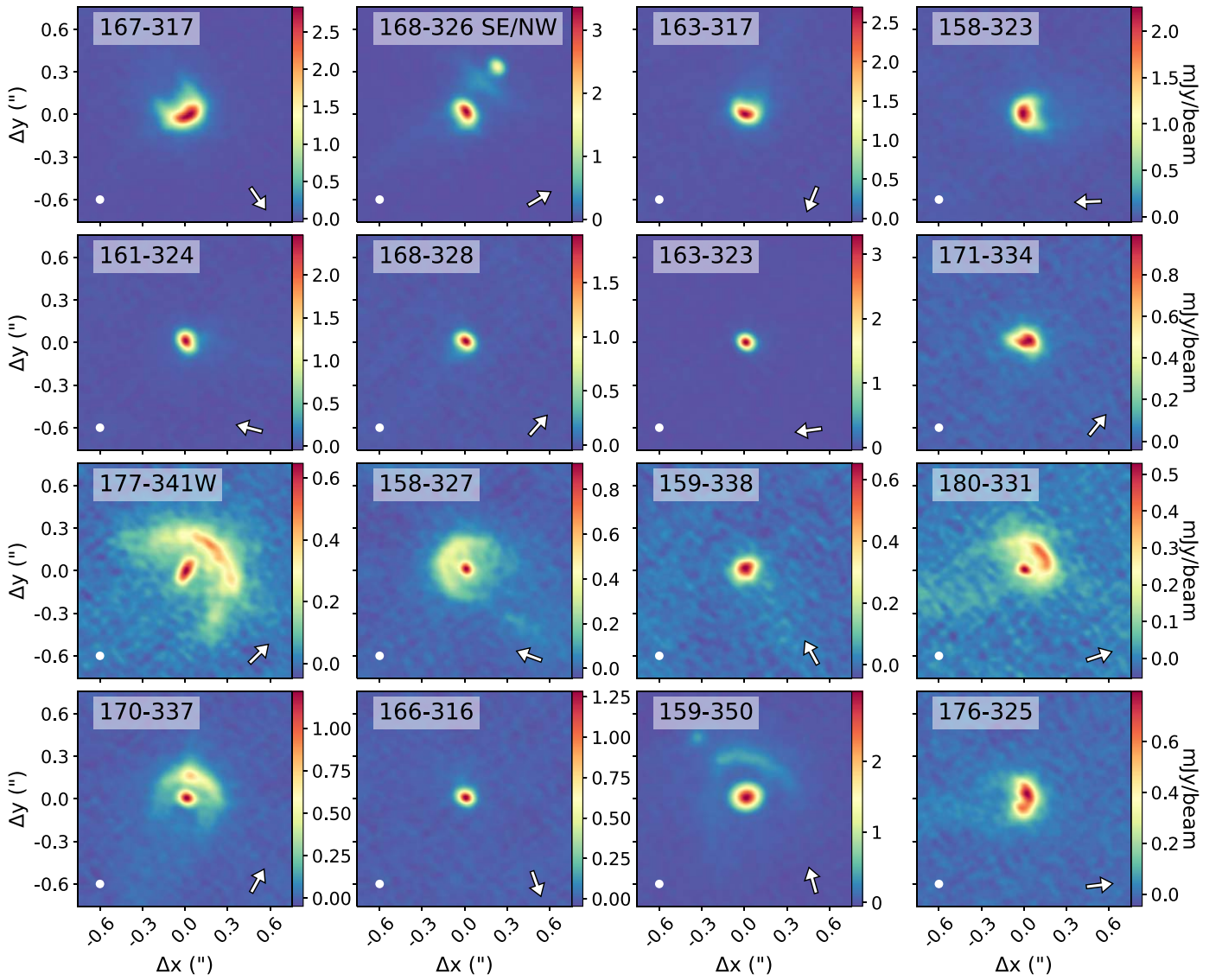
Figure 11. The 3.1 mm continuum images of H41α-detected proplyds in the ONC. Each image is generated as a subimage from the larger 3.1 mm continuum mosaic from N. P. Ballering et al. (2023). The synthesized beam is shown in the bottom left corner of each panel. The arrow in each panel points to the direction of θ^1 Ori C.

Appendix B
Additional Spectra Plots

Here, we include Figure 12, which shows zoomed-in radio recombination line spectral for proplyds 168–328, 163–323, 166–316, and 176–325.

We also include Figure 13, which plots best-fit Gaussian and Voigt profiles for the highest-S/N detection in our sample, proplyd 167–317. Gaussian and Voigt profile fitting are both performed using pyspeckit (A. Ginsburg et al. 2022). Both fits yield similar reduced χ^2 values, but differ in the velocity channels that are away from the best-fit central velocities and where the signal-to-noise ratio is the lowest.
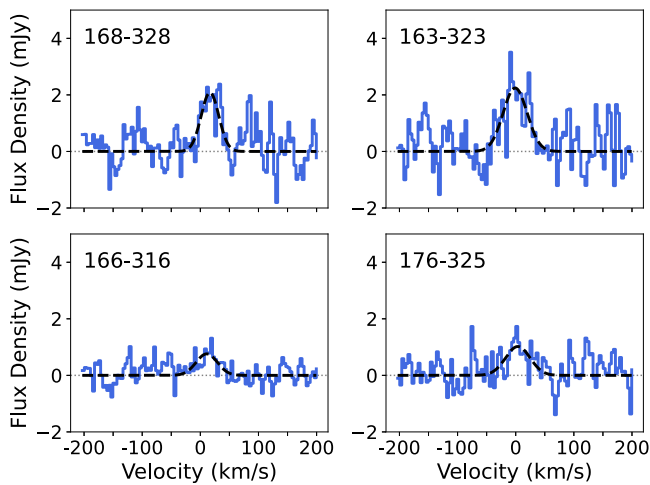
Figure 12. Zoomed-in radio recombination line spectra (blue lines) and best-fit Gaussian line profiles (black lines) for proplyds 168–328, 163–323, 166–316, and 176–325. These spectra and line profiles are also shown in Figure 4, except here we use smaller *y*-axis limits.
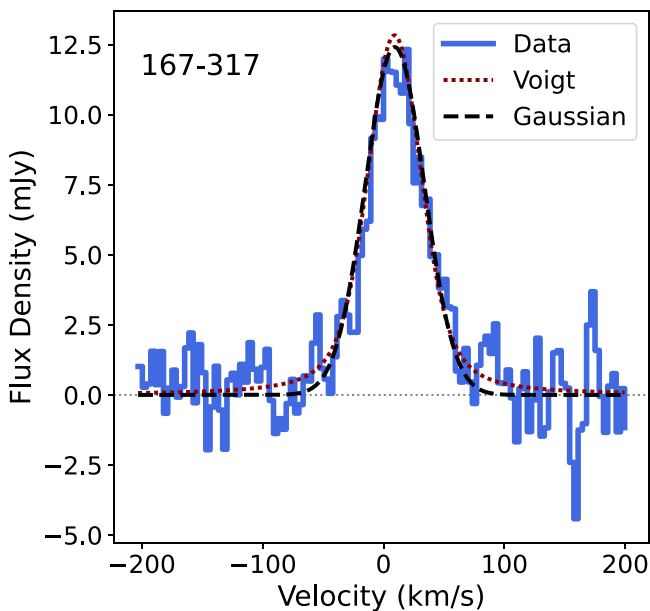

Figure 13. Radio recombination line spectrum (solid blue line), best-fit Gaussian line profile (dashed black line), and best-fit Voigt line profile (dotted brown line) for proplyd 167–317.

ORCID iDs

Ryan D. Boyden https://orcid.org/0000-0001-9857-1853
Kimberly L. Emig https://orcid.org/0000-0001-6527-6954
Nicholas P. Ballering https://orcid.org/0000-0002-4276-3730
Charles J. Law https://orcid.org/0000-0003-1413-1776
Thomas J. Haworth https://orcid.org/0000-0002-9593-7618
Jonathan C. Tan https://orcid.org/0000-0002-3389-9142
L. Ilsedore Cleeves https://orcid.org/0000-0003-2076-8001
Zhi-Yun Li https://orcid.org/0000-0002-7402-6487

References

Adams, F. C. 2010, ARA&A, 48, 47
Adams, F. C., Hollenbach, D., Laughlin, G., & Gorti, U. 2004, ApJ, 611, 360
Anderson, L. D., Bania, T. M., Balser, D. S., & Rood, R. T. 2011, ApJS, 194, 32
Anglada, G., Rodríguez, L. F., & Carrasco-González, C. 2018, A&ARv, 26, 3
Aru, M.-L., Mauco, K., Manara, C. F., et al. 2024, A&A, 687, A93
Astropy Collaboration, Price-Whelan,, A. M., Lim, P. L., et al. 2022, ApJ, 935, 167
Astropy Collaboration, Price-Whelan, A. M., Sipőcz, B. M., et al. 2018, AJ, 156, 123
Astropy Collaboration, Robitaille, T. P., Tollerud, E. J., et al. 2013, A&A, 558, A33
Baldwin, J. A., Ferland, G. J., Martin, P. G., et al. 1991, ApJ, 374, 580
Ballering, N. P., Cleeves, L. I., Boyden, R. D., et al. 2025, ApJ, 979, 110
Ballering, N. P., Cleeves, L. I., Haworth, T. J., et al. 2023, ApJ, 954, 127
Bally, J., Mann, R. K., Eisner, J., et al. 2015, ApJ, 808, 69
Bally, J., O'Dell, C. R., & McCaughrean, M. J. 2000, AJ, 119, 2919
Bally, J., Sutherland, R. S., Devine, D., & Johnstone, D. 1998, AJ, 116, 293
Bally, J., Youngblood, A., & Ginsburg, A. 2012, ApJ, 756, 137
Balser, D. S., & Wenger, T. V. 2024, ApJ, 964, 47
Bergin, E. A., Alexander, C., Drozdovskaya, M., Gounelle, M., & Pfalzner, S. 2023, arXiv:2301.05212
Berné, O., Habart, E., Peeters, E., et al. 2024, Sci, 383, 988
Bik, A., Lenorzer, A., Kaper, L., et al. 2003, A&A, 404, 249
Boyden, R. D., & Eisner, J. A. 2020, ApJ, 894, 74
Boyden, R. D., & Eisner, J. A. 2023, ApJ, 947, 7
Boyden, R. D., & Eisner, J. A. 2024, ApJ, 967, 103
Brocklehurst, M., & Seaton, M. J. 1972, MNRAS, 157, 179
CASA Team, Bean, B., Bhatnagar, S., et al. 2022, PASP, 134, 114501
Churchwell, E. 2002, ARA&A, 40, 27
Churchwell, E., Felli, M., Wood, D. O. S., & Massi, M. 1987, ApJ, 321, 516
Churchwell, E., Mezger, P. G., & Huchtmeier, W. 1974, A&A, 32, 283
Clarke, C. J. 2007, MNRAS, 376, 1350
Coleman, G. A. L., & Haworth, T. J. 2022, MNRAS, 514, 2315
Coleman, G. A. L., Mroueh, J. K., & Haworth, T. J. 2024, MNRAS, 527, 7588
Comrie, A., Wang, K.-S., Hsu, S.-C., et al. 2021, CARTA: The Cube Analysis and Rendering Tool for Astronomy, v2.0.0, Zenodo, doi:10.5281/zenodo.3377984
Concha-Ramírez, F., Wilhelm, M. J. C., & Portegies Zwart, S. 2023, MNRAS, 520, 6159
Concha-Ramírez, F., Wilhelm, M. J. C., Portegies Zwart, S., & Haworth, T. J. 2019, MNRAS, 490, 5678
Concha-Ramírez, F., Wilhelm, M. J. C., Portegies Zwart, S., van Terwisga, S. E., & Hacar, A. 2021, MNRAS, 501, 1782
Draine, B. T. 2011, Physics of the Interstellar and Intergalactic Medium (Princeton, NJ: Princeton Univ. Press)
Eisner, J. A., Arce, H. G., Ballering, N. P., et al. 2018, ApJ, 860, 77
Eisner, J. A., Plambeck, R. L., Carpenter, J. M., et al. 2008, ApJ, 683, 304
Emig, K. L. 2021, PhD thesis, Univ. Leiden
Emig, K. L., Bolatto, A. D., Leroy, A. K., et al. 2020, ApJ, 903, 50
Facchini, S., Clarke, C. J., & Bisbas, T. G. 2016, MNRAS, 457, 3593
Factor, S. M., Hughes, A. M., Flaherty, K. M., et al. 2017, AJ, 153, 233
Fang, M., Kim, J. S., Pascucci, I., & Apai, D. 2021, ApJ, 908, 49
Forbrich, J., Rivilla, V. M., Menten, K. M., et al. 2016, ApJ, 822, 93
Galván-Madrid, R., Díaz-González, D. J., Motte, F., et al. 2024, ApJS, 274, 15
Galván-Madrid, R., Zhang, Q., Izquierdo, A., et al. 2023, ApJL, 942, L7
Gárate, M., Pinilla, P., Haworth, T. J., & Facchini, S. 2024, A&A, 681, A84
Garay, G., Lizano, S., Gómez, Y., & Brown, R. L. 1998, ApJ, 501, 710
Garay, G., Moran, J. M., & Reid, M. J. 1987, ApJ, 314, 535
Gautam, A., Farias, J. P., & Tan, J. C. 2025, MNRAS, 536, 298
Ginsburg, A., Sokolov, V., de Val-Borro, M., et al. 2022, AJ, 163, 291
Goicoechea, J. R., Le Bourlot, J., Black, J. H., et al. 2024, A&A, 689, L4
Gordon, M. A., & Sorochenko, R. L. 2009, Radio Recombination Lines. Their Physics and Astronomical Applications (Berlin: Springer)
Großschedl, J. E., Alves, J., Meingast, S., et al. 2018, A&A, 619, A106
Habart, E., Peeters, E., Berné, O., et al. 2024, A&A, 685, A73
Haworth, T. J. 2021, MNRAS, 503, 4172
Haworth, T. J., & Clarke, C. J. 2019, MNRAS, 485, 3895
Haworth, T. J., Clarke, C. J., Rahman, W., Winter, A. J., & Facchini, S. 2018a, MNRAS, 481, 452
Haworth, T. J., Facchini, S., Clarke, C. J., & Mohanty, S. 2018b, MNRAS, 475, 5460
Haworth, T. J., Harries, T. J., Acreman, D. M., & Bisbas, T. G. 2015, MNRAS, 453, 2277
Haworth, T. J., Kim, J. S., Winter, A. J., et al. 2021, MNRAS, 501, 3502
Haworth, T. J., & Owen, J. E. 2020, MNRAS, 492, 5030
Henney, W. J., & Arthur, S. J. 1998, AJ, 116, 322
Henney, W. J., & O'Dell, C. R. 1999, AJ, 118, 2350
Henney, W. J., O'Dell, C. R., Meaburn, J., Garrington, S. T., & Lopez, J. A. 2002, ApJ, 566, 315

Hildebrand, R. H. 1983, QJRAS, 24, 267
Hillenbrand, L. A. 1997, AJ, 113, 1733
Hirota, T., Bushimata, T., Choi, Y. K., et al. 2007, PASJ, 59, 897
Huang, S., Portegies Zwart, S., & Wilhelm, M. J. C. 2024, A&A, 689, A338
Hunter, J. D. 2007, CSE, 9, 90
Jiménez-Serra, I., Báez-Rubio, A., Martín-Pintado, J., Zhang, Q., & Rivilla, V. M. 2020, ApJL, 897, L33
Johnstone, D., Hollenbach, D., & Bally, J. 1998, ApJ, 499, 758
Keppler, M., Benisty, M., Müller, A., et al. 2018, A&A, 617, A44
Keto, E., Zhang, Q., & Kurtz, S. 2008, ApJ, 672, 423
Kim, J. S., Clarke, C. J., Fang, M., & Facchini, S. 2016, ApJL, 826, L15
Kirwan, A., Manara, C. F., Whelan, E. T., et al. 2023, A&A, 673, A166
Klaassen, P. D., Johnston, K. G., Urquhart, J. S., et al. 2018, A&A, 611, A99
Kounkel, M., Covey, K., Suárez, G., et al. 2018, AJ, 156, 84
Kounkel, M., Hartmann, L., Mateo, M., & Bailey, J. I. I. 2017, ApJ, 844, 138
Kraus, S., Balega, Y. Y., Berger, J. P., et al. 2007, A&A, 466, 649
Krumholz, M. R., McKee, C. F., & Bland-Hawthorn, J. 2019, ARA&A, 57, 227
Lada, C. J., & Lada, E. A. 2003, ARA&A, 41, 57
Lada, E. A., Strom, K. M., & Myers, P. C. 1993, in Protostars and Planets III, ed. E. H. Levy & J. I. Lunine (Tucson, AZ: Univ. of Arizona Press), 245
Liu, X., Liu, T., Shen, Z., et al. 2023, A&A, 671, L1
Mann, R. K., Di Francesco, J., Johnstone, D., et al. 2014, ApJ, 784, 82
Martínez-Henares, A., Zhang, Q., Jiménez-Serra, I., et al. 2024, ApJL, 971, L7
McCaughrean, M. J., & Pearson, S. G. 2023, arXiv:2310.03552
Méndez-Delgado, J. E., Esteban, C., García-Rojas, J., & Henney, W. J. 2022, MNRAS, 514, 744
Méndez-Delgado, J. E., Esteban, C., García-Rojas, J., Kreckel, K., & Peimbert, M. 2023, Natur, 618, 249
Méndez-Delgado, J. E., Esteban, C., García-Rojas, J., et al. 2021, MNRAS, 502, 1703
Menten, K. M., Reid, M. J., Forbrich, J., & Brunthaler, A. 2007, A&A, 474, 515
Mesa-Delgado, A., Núñez-Díaz, M., Esteban, C., et al. 2012, MNRAS, 426, 614
Mezger, P. G., & Henderson, A. P. 1967, ApJ, 147, 471
Moscadelli, L., Cesaroni, R., Beltrán, M. T., & Rivilla, V. M. 2021, A&A, 650, A142
Ndugu, N., Bitsch, B., & Jurua, E. 2018, MNRAS, 474, 886
Nicholson, R. B., Parker, R. J., Church, R. P., et al. 2019, MNRAS, 485, 4893
Öberg, K. I., & Bergin, E. A. 2021, PhR, 893, 1
Öberg, K. I., Facchini, S., & Anderson, D. E. 2023, ARA&A, 61, 287
O'Dell, C. R., Kollatschny, W., & Ferland, G. J. 2017, ApJ, 837, 151
O'dell, C. R., & Wen, Z. 1994, ApJ, 436, 194
Otter, J., Ginsburg, A., Ballering, N. P., et al. 2021, ApJ, 923, 221

Pabst, C. H. M., Goicoechea, J. R., Cuadrado, S., et al. 2024, A&A, 688, A7
Parker, R. J. 2020, RSOS, 7, 201271
Parker, R. J., Alcock, H. L., Nicholson, R. B., Panić, O., & Goodwin, S. P. 2021a, ApJ, 913, 95
Parker, R. J., Nicholson, R. B., & Alcock, H. L. 2021b, MNRAS, 502, 2665
Peimbert, M., Ukita, N., Hasegawa, T., & Jugaku, J. 1988, PASJ, 40, 581
Peterson, D. E., & Megeath, S. T. 2008, in Handbook of Star Forming Regions, Volume I, ed. B. Reipurth (San Francisco, CA: ASP Monograph), 590
Prasad, S., Zhang, Q., Moran, J., et al. 2023, ApJL, 953, L6
Purser, S. J. D., Lumsden, S. L., Hoare, M. G., et al. 2016, MNRAS, 460, 1039
Qiao, L., Coleman, G. A. L., & Haworth, T. J. 2023, MNRAS, 522, 1939
Qiao, L., Haworth, T. J., Sellek, A. D., & Ali, A. A. 2022, MNRAS, 512, 3788
Ricci, L., Robberto, M., & Soderblom, D. R. 2008, AJ, 136, 2136
Richling, S., & Yorke, H. W. 2000, ApJ, 539, 258
Roshi, D. A., Churchwell, E., & Anderson, L. D. 2017, ApJ, 838, 144
Sandstrom, K. M., Peek, J. E. G., Bower, G. C., Bolatto, A. D., & Plambeck, R. L. 2007, ApJ, 667, 1161
Scally, A., & Clarke, C. 2001, MNRAS, 325, 449
Shaver, P. A., McGee, R. X., Newton, L. M., Danks, A. C., & Pottasch, S. R. 1983, MNRAS, 204, 53
Sheehan, P. D., Eisner, J. A., Mann, R. K., & Williams, J. P. 2016, ApJ, 831, 155
Störzer, H., & Hollenbach, D. 1999, ApJ, 515, 669
Throop, H. B., & Bally, J. 2005, ApJL, 623, L149
Tsamis, Y. G., Flores-Fajardo, N., Henney, W. J., Walsh, J. R., & Mesa-Delgado, A. 2013, MNRAS, 430, 3406
Tsamis, Y. G., & Walsh, J. R. 2011, MNRAS, 417, 2072
Tsamis, Y. G., Walsh, J. R., Vílchez, J. M., & Péquignot, D. 2011, MNRAS, 412, 1367
Vasconcelos, M. J., Cerqueira, A. H., Plana, H., Raga, A. C., & Morisset, C. 2005, AJ, 130, 1707
Walsh, C., Millar, T. J., & Nomura, H. 2013, ApJL, 766, L23
Wenger, T. V., Balser, D. S., Anderson, L. D., & Bania, T. M. 2019, ApJ, 887, 114
Wilhelm, M. J. C., Portegies Zwart, S., Cournoyer-Cloutier, C., et al. 2023, MNRAS, 520, 5331
Winter, A. J., Clarke, C. J., Rosotti, G., et al. 2018, MNRAS, 478, 2700
Winter, A. J., & Haworth, T. J. 2022, EPJP, 137, 1132
Winter, A. J., Haworth, T. J., Coleman, G. A. L., & Nayakshin, S. 2022, MNRAS, 515, 4287
Winter, A. J., Kruijssen, J. M. D., Chevance, M., Keller, B. W., & Longmore, S. N. 2020, MNRAS, 491, 903
Zannese, M., Tabone, B., Habart, E., et al. 2024, NatAs, 8, 577
Zapata, L. A., Rodríguez, L. F., Kurtz, S. E., & O'Dell, C. R. 2004, AJ, 127, 2252